Rock Mechanics Bulletin 5 (2026) 100271

Contents lists available at ScienceDirect

Rock Mechanics Bulletin

journal homepage: www.keaipublishing.com/en/journals/rock-mechanics-bulletin

A method for evaluating the stability of roadway surrounding rock based on a modified damage evolution characteristic model considering rock mass residual strength and 3D DEM

Shengrong Xie[a], Yuxuan Wang[a], Yiyi Wu[a,b,c,*], Jian Yang[a], Zhigen Wang[d]

[a] School of Energy and Mining Engineering, China University of Mining & Technology (Beijing), Beijing, 100083, China
[b] State Key Laboratory for Tunnel Engineering, China University of Mining and Technology (Beijing), Beijing, 100083, China
[c] College of Construction Engineering, Jilin University, Changchun, 130021, China
[d] China Coal Huayu Nanyangpo Coal Industry Co., Ltd., Shuozhou, 036999, China

ARTICLE INFO

Keywords:
Multi-seam mining
Modified damage evolution characteristic model
Three-dimensional discrete element method (3D DEM)
Coal pillar width
Fracture line position

ABSTRACT

Repetitive mining in multi-seam conditions induces cumulative damage to surrounding rock, significantly increasing the risk of roadway instability. Taking the roadway in the extra-thick coal seam fully mechanized top-coal caving face as the research object, this study innovatively developed a modified damage evolution characteristic model that considers the residual strength of rock mass to quantify the regulatory effect of damage variable D on roof fracture span: damage to the main roof reduces the initial and periodic fracture spans, significantly increasing the probability of sliding and rotational instability of the voussoir beam structure. On this basis, a three-dimensional discrete element method (3D DEM) model was established, and orthogonal tests were designed to reveal the coupling mechanism of the spatial position of fracture lines and coal pillar width on rock mass damage. The results show that when the coal pillar width increases from 8 m to 16 m, the peak stress at the roadway ribs decreases by 26.5%–43.3%, and the influence range of the second invariant of the deviatoric stress tensor (J_2) shrinks. The attenuation of stress gradient leads to a decrease in the evolution rate of plastic damage with increasing coal pillar width, while the position of the fracture line has a weak regulatory effect on the stress-plastic response of the coal pillar. The results of theoretical analysis and 3D DEM simulations have effectively guided on-site engineering practice.

1. Introduction

With the intensification of coal resource extraction in China, single-seam resources with favorable geological conditions have gradually been depleted (Cheng et al., 2020; Zhang et al., 2024b). Cumulative damage effects resulting from repeated mining in multi-seam configurations have become increasingly prominent, posing a critical challenge to safe and efficient mining operations (Qin et al., 2021; Wang et al., 2021b). The stress field induced by upper coal seam extraction inevitably causes damage to the floor strata (Huang et al., 2021; Wang et al., 2024; Zhu and Tu, 2017). The interlayer rock mass experiences cyclic stress reinforcement-decompression disturbances, leading to weakened integrity and bearing capacity of the roof structure during subsequent lower-seam mining. This degradation process often results in instability of key bearing structures within the voussoir beam system, triggering large-scale dynamic pressure manifestations and associated hazards in working faces (Liu et al., 2024b; Mark, 2021; Ning et al., 2020). Additionally, when the distance between goaf areas of adjacent working faces is insufficient, the degree of differential degradation in surrounding rock caused by historical mining activities in upper seams directly affects the rational design of barrier pillar widths. This creates significant challenges for maintaining stope stability and controlling roadway deformations under such complex stress conditions (Chen et al., 2022; Liu et al., 2022; Zhang et al., 2021).

Under close-distance multi-seam mining conditions, mining disturbances from upper coal seams induce redistribution of the in-situ stress field within interlayer rock masses. During subsequent lower-seam extraction, the presence of microcracks and macroscopic fractures in the roof leads to alterations in roof failure mechanisms (Lu et al., 2019; Zhao et al., 2021). Therefore, understanding the fracturing mechanism

* Corresponding author.
E-mail address: 15662045768@163.com (Y. Wu).
Peer review under the responsibility of Chinese Society for Rock Mechanics & Engineering.

https://doi.org/10.1016/j.rockmb.2025.100271
Received 24 July 2025; Received in revised form 15 September 2025; Accepted 1 November 2025
Available online 6 November 2025

of interlayer rock masses is fundamental to revealing strata behavior characteristics during lower-seam mining. Scholars worldwide have conducted systematic studies. Li et al. (2022b) identified that cantilever beam structure instability in multi-seam mining roofs is the primary cause of roof fall accidents. Guo et al. (2021) uncovered a critical correlation between the tensile strengths of immediate and main roofs and failure modes in solid coal side roadways. Liu et al. (2024a) clarified the evolutionary law of mining-induced fractures in composite roofs based on the hard rock proportional coefficient. Zhang et al. (2024a) established mechanical criteria for rockburst initiation triggered by instability in composite hard roof structures. These studies demonstrate that roof failure modes significantly modulate dynamic stress field evolution, while repeated mining operations also promote upward propagation of fractures, driving continuous migration and evolution of overlying strata structures (Bai et al., 2019; Suchowerska Iwanec et al., 2016; Yang et al., 2019). Ghabraie et al. (2017a; b) proposed a subsidence prediction method considering multi-seam mining characteristics, whereas Li et al. (2024) achieved precise surface subsidence analysis through coupled physical-numerical simulation approaches. Following upper-seam extraction, special roadway layouts such as gob-side entry driving (Wang et al., 2021a; Xie et al., 2024), gob-side entry retaining (Han et al., 2019; Hu et al., 2024), or narrow-pillar roadway support (Li et al., 2022a; Zha et al., 2017) may be adopted in lower seams under specific geological conditions. These configurations create complex geo-mechanical environments with significant spatial stress distribution heterogeneities. Stress transfer channels formed by pillar cracks and roof delamination spaces often lead to failures in bolt-cable support systems (Wang et al., 2016) and excessive roof convergence (Geng et al., 2024). To address these technical challenges, Wang et al. (2023) developed bidirectional grouting anchor cables for reinforcing 4 m narrow pillars, successfully maintaining roadway deformations within safety limits in field applications. Chen et al. (2023) implemented flexible formwork concrete wall backfilling technology at Daliuta Coal Mine. Wu et al. (2023) proposed a staged collaborative support strategy based on zonal damage characteristics of surrounding rocks in gently inclined close-distance seams.

In summary, repeated mining in multi-seam configurations results in cumulative damage to roadway surrounding rocks and alterations in stress environments. This study focuses on roadways subjected to multiple mining disturbances in the extra-thick coal seam fully mechanized caving face of Nanyangpo Mine. It identifies that stress field reconstruction induced by extremely close upper-seam mining and the influence of large-span hanging roof structures in adjacent goafs are the dominant controlling factors leading to degradation and instability of the surrounding rock bearing system. By developing a modified damage evolution characteristic model incorporating rock residual strength, the multi-scale damage evolution mechanism of interlayer main roof strata is systematically elucidated. Based on 3D DEM modeling and orthogonal experiments, quantitative simulations are conducted to analyze the spatiotemporal evolution characteristics of surrounding rock stress fields and plastic zones under the coupling effects of fracture line spatial positions and pillar widths. The optimal pillar width of 12 m is comprehensively determined through this analysis. Subsequently, a corresponding control technology system for surrounding rock stability is established, which achieved favorable results in field industrial tests. The findings provide theoretical guidance and engineering references for surrounding rock control in roadways subjected to multiple disturbances under similar geological conditions.

2. Research background

2.1. Analysis of geological plan

Nanyangpo Coal Mine is located in Shuozhou City, Shanxi Province, with the main mining target being the 4–6 coal seams. The current mining face is the 26110 longwall top coal caving working face in No. 6 seam. Geological surveys indicate that this face is vertically separated by 27.85 m from the overlying 4^{-2} coal seam, which itself is separated by 6.2 m from the 4^{-1} coal seam, representing typical multi-seam repeated mining geological conditions. The mining area has a burial depth of 217 m–265 m, with an average coal seam dip angle of 3° and mean thickness of 11.9 m. The working face is characterized by an east-high-west-low monocline structure with gently dipping strata, and contains no abnormal structures such as faults or collapse columns. The layout of the working face is presented in Fig. 1.

This study focuses on the 26,110 tailgate as the research object, with a roadway cross-section of 4.8 m × 3.5 m. The 24202 gob area of the 4^{-2} coal seam is located above, and the southern side is adjacent to the 26,112 working face. Owing to significant repeated mining disturbances from multiple overlying coal seams during extraction, cumulative damage effects in surrounding rocks have increased the complexity of roadway support. Furthermore, due to the close proximity between the 26,110 tailgate and the gob, determining the optimal width of the sectional coal pillar between the 26110 tailgate and the 26112 headgate is of critical importance for safe and efficient mining operations.

2.2. Columnar configuration of coal and rock strata

The No.6 coal seam exhibits a monolithic structure with an average thickness of 11.9 m, containing approximately 0.2 m of gangue. The immediate roof consists of coarse grained sandstone with an average thickness of 1.61 m, overlain by a dense and hard medium grained sandstone main roof measuring 8.94 m in average thickness. The immediate floor is composed of fine grained sandstone with an average thickness of 2.55 m. The stratigraphic occurrence characteristics of coal and rock formations are illustrated in Fig. 2.

2.3. Key challenges in controlling damaged surrounding rock

To address the specific operational conditions of the 26,110 tailgate under the combined effects of multi-seam repeated mining and residual stress on the adjacent gob side, the roadway must maintain relative stability from its formation to the end of working face mining, minimizing maintenance requirements. The six key control challenges for fully mechanized caving roadways are illustrated in Fig. 3: (1) Cumulative damage accumulation in the main roof induced by multi-seam repeated mining, leading to progressive micro-fracture development and eventual large-scale macro-damage. (2) Stress perturbations from roadway excavation causing localized plastic failure in specific areas. (3) Asymmetric abutment pressure fields within coal pillars due to lateral stress from adjacent panel mining, exacerbating plasticization and reducing support capacity. (4) Multi-modal extrusion deformation resulting from overburden rotation-subsidence structural movements when the main roof is at different fracture positions (gob, coal pillar, roadway, solid coal). (5) Determination of optimal coal pillar width: narrow pillars improve recovery but compromise stability, while wider pillars waste resources. (6) Unpredictable mining pressure behavior and risks due to the superposition of historical mining damage and intense current panel mining disturbances.

3. Multi-scale damage evolution mechanism of main roof interlayer strata

3.1. Damage categories of interlayer main roof strata

Based on the correlation analysis between damage mechanics characteristics and overburden structural evolution, the interlayer main roof damage during working face advancement can be classified into three categories, as illustrated in Fig. 4.

(1) No damage stable type: The main roof lies at a greater distance from the upper coal seam and remains outside the floor plastic

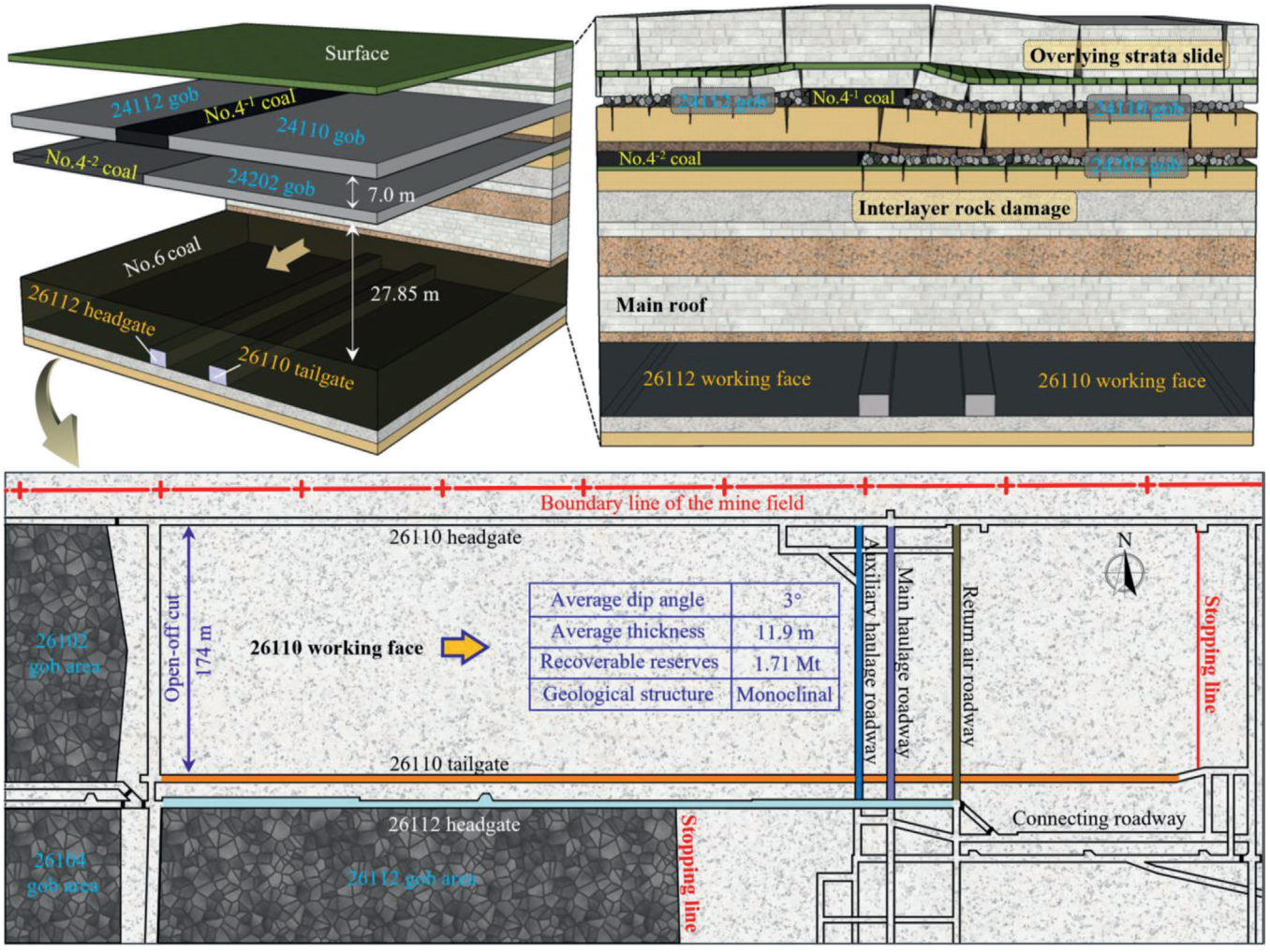

Fig. 1. General layout of 26110 working face.

failure zone, maintaining an intact structure without significant disturbance. (2) Gradient damage transition type: The floor plastic failure zone of the upper coal seam intrudes into the main roof, forming a damage gradient layer with a certain depth. (3) Penetrative damage instability type: The main roof undergoes complete damage, where progressive micro-fracture development results in the formation of penetrative macrocracks and a substantial reduction in load-bearing capacity.

3.2. Modified damage relation based on equivalent strain theory

Within the framework of continuum damage mechanics theory, the essence of damage evolution in rock materials is characterized by the progressive failure process of microscopic elements under meso-scale stress fields. In three-dimensional stress states, the damage variable is defined as the ratio of the equivalent damaged area to the original intact cross-sectional area within a representative elementary volume, expressed as follows,

$$D = 1 - \frac{\tilde{A}}{A} \tag{1}$$

where D is the damage variable ($0 \le D \le 1$), $\tilde{A}$ is the effective load-bearing area, and A is the nominal (initial) area.

According to Lemaitre's equivalent strain theory, the strain generated in damaged materials ($D \neq 0$) under effective stress is equivalent to the strain of undamaged materials ($D = 0$) under nominal stress (Lemaitre et al., 1999), as illustrated in Fig. 5. Based on this principle, the effective stress in damaged materials can be substituted for the initial nominal stress, with the mathematical expression,

$$\varepsilon = \frac{\tilde{\sigma}}{E} = \frac{\sigma}{E(1-D)} = \frac{\sigma}{\tilde{E}} \tag{2}$$

where ε is the strain, $\tilde{\sigma}$ is the effective stress, σ is the initial stress, E is the elastic modulus of undamaged materials, and $\tilde{E}$ is the damaged elastic modulus. Through transformation, the expression for $\tilde{\sigma}$ can be derived as,

$$\tilde{\sigma} = \frac{\sigma}{1-D} = \frac{E\varepsilon}{1-D} \tag{3}$$

Within the theoretical framework of rock damage mechanics, although the isotropic damage assumption imposes spatial uniformity on the damage variable D, the damage evolution inherently exhibits significant anisotropy due to the directional arrangement of mineral grains and fractured pore structures during diagenesis. The mechanical evolution of interlayer rock mass damage can be divided into three stages: elastic stage, plastic stage, and macroscopic fracture stage. Classical equivalent strain theory assumes that voids form within the rock mass during the plastic and fracture stages, rendering the rock unable to sustain mechanical loads. However, in reality, rock retains residual strength after micro-element failure and can still transmit normal compressive stress and shear stress components, indicating that traditional models overestimate damage degradation. In light of this,

Lithology	Thickness/m	Depth/m	Lithology description
Medium grained sandstone	8.37	210.27	Grayish white, thick layered, mainly composed of quartz, followed by feldspar in other minerals, sub-round, with average sorting.
Mudstone	0.98	211.25	Dark gray, blocky, brittle and fragile in nature.
Medium grained sandstone	3.04	214.29	Grayish white, mainly composed of quartz, followed by feldspar, sub-round, well sorted.
No.4^{-1} Coal	**2.91**	**217.20**	**Black, blocky, weak glassy luster, uneven fractures.**
Siltstone	5.50	222.70	Light gray, horizontal bedding, well-developed joints.
Carbonaceous mudstone	1.50	224.20	Dark gray, blocky.
No.4^{-2} Coal	**2.31**	**226.51**	**Black, fragmented, semi-dark coal.**
Mudstone	0.70	227.21	Black, fragmented.
Siltstone	3.26	230.47	Dark gray, horizontally layered, with scratches, well-developed joints.
Fine grained sandstone	4.88	235.35	Gray white, thick layered, mainly composed of feldspar, poorly sorted, and the rock core is relatively fragmented.
Medium grained sandstone	2.30	237.65	Light gray, thick layered, with developed cracks and broken core.
Coarse grained sandstone	6.24	243.89	Grayish white, thick layered, mainly composed of quartz, sub-round, and generally sorted.
Medium grained sandstone	8.94	252.83	Light gray, thick layered, mainly composed of quartz, sub-circular, and generally sorted.
Coarse grained sandstone	1.61	254.44	Grayish white, thick layered, mainly composed of feldspar, followed by quartz, sub-round, and moderately sorted.
No.6 Coal	**11.90**	**266.34**	**Black, blocky, with weak glass luster, uniform and uneven fracture.**
Fine grained sandstone	2.55	268.89	Grayish white, mainly composed of feldspar, followed by quartz sub-round, and generally sorted.
Siltstone	2.20	271.09	Dark gray, horizontal bedding, developed joints.

Fig. 2. Stratigraphic occurrence characteristics of coal and rock strata.

this study introduces a damage correction coefficient ξ ($0 \le \xi \le 1$) to establish a modified damage evolution characteristic model for rock based on equivalent strain theory.

$$\tilde{\sigma} = \frac{\sigma}{1-\xi D} = \frac{E\varepsilon}{1-\xi D} \tag{4}$$

The core physical meaning of the ξ is to characterize the contribution ratio of residual strength to the overall bearing capacity of rock mass after micro-element failure of rock. The classical equivalent strain theory assumes that rock completely loses its bearing capacity after damage, such as microcrack development and local fragmentation. However, in actual engineering, even if local micro-element failure occurs in rock, part of the residual strength is still retained, which can transmit normal compressive stress and shear stress. The introduction of ξ is precisely to quantify the contribution degree of residual strength: when $\xi = 1$, it indicates that rock completely loses residual strength after damage, which is consistent with the assumption of classical theory; when $\xi = 0$, it indicates that the residual strength of rock does not attenuate after damage, still maintaining the bearing capacity of intact rock mass. In actual value selection, the closer ξ is to 1, the weaker the residual strength of rock after damage, the higher the degree of rock mass fragmentation, and the more significant the deterioration of bearing capacity; conversely, the smaller ξ is, the more significant the contribution of residual strength to bearing capacity. The value of ξ can be obtained via uniaxial compression tests, by recording the peak strength σ_p and residual strength σ_r; the initial value of ξ is the ratio of residual strength to peak strength, i.e., $\xi = \sigma_r/\sigma_p$. The parameter ξ captures the heterogeneity and nonlinear characteristics of rock materials, enabling precise characterization of the rock mass damage process.

3.3. Mechanical evolution process of interlayer rock mass damage

(1) Analysis of first fracture damage state of main roof

During the strike-wise advancement of the working face, the exposed area of the main roof continuously increases until reaching the critical breaking length and fracturing. For longwall faces, the main roof typically exhibits a vertical "O-X" type fracture. Therefore, the first fracture of the main roof is simplified as a two-dimensional (2D) fixed-fixed beam model with elastic foundation constraints, as presented in Fig. 6.

Where L is the beam length, h is the beam height, and q is the uniformly distributed load on the beam.

Based on elastic mechanics theory, the horizontal stress is obtained as shown in Eq. (5) (Xie et al., 2022), where υ denotes the Poisson's ratio of the beam.

$$\sigma_x = \frac{qy}{h^3}\left(4y^2 - 6x^2 + 6xL - L^2\right) + \frac{3(2\nu-1)qy}{5h} - \frac{1}{2}\nu q \tag{5}$$

Eq. (5) indicates that the uniformly distributed load q on the fixed-fixed beam only alters the stress magnitude without changing its distribution characteristics, as shown in Fig. 7. Based on the equivalent strain hypothesis, although the elastic modulus of damaged rock decreases, Poisson's ratio remains constant. Therefore, the horizontal stress distribution on the beam is solely dependent on the thickness h and span L. In this study, with a uniformly distributed load $q = 1$ MPa, Poisson's ratio $\upsilon = 0.2$, and beam height $h = 10$ m, the horizontal stress

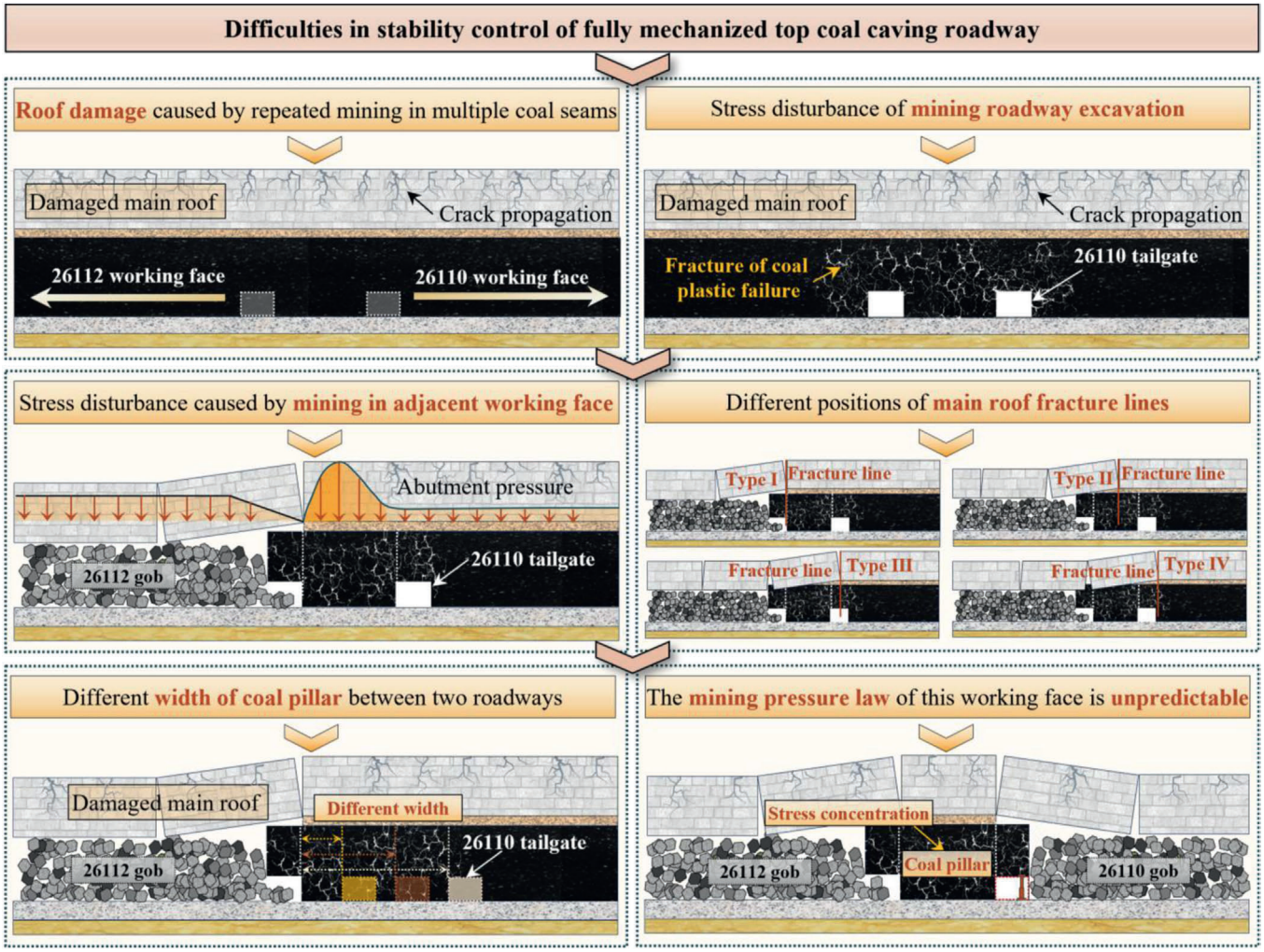

Fig. 3. Control challenges of damaged surrounding rock in 26110 tailgate.

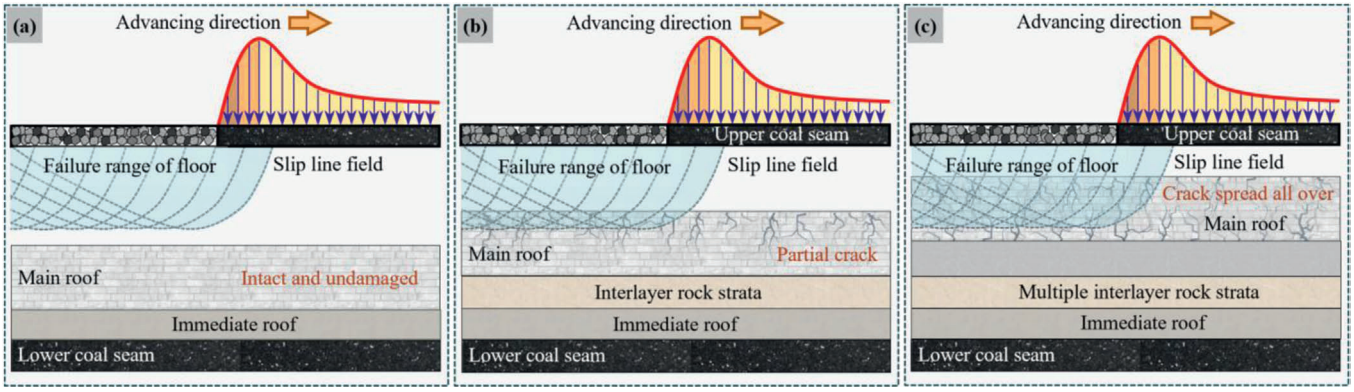

Fig. 4. Different damage categories of main roof strata. (a) No damage stable type, (b) Gradient damage transition type, (c) Penetrative damage instability type.

distribution within the fixed-fixed beam was analyzed for six span conditions: $L = 12$ m, 14 m, 16 m, 18 m, 20 m, and 22 m.

According to material mechanics theory, with increasing exposed roof area, the maximum bending moment of the fixed-fixed beam under uniform load is concentrated in the end constraint regions. When the horizontal tensile stress exceeds the tensile strength limit of the rock beam, tension-dominated brittle fracture occurs. Therefore, the tensile strength limit of the damaged main roof is,

$$\tilde{\sigma} = \frac{\sigma}{1 - \xi D} \leq [\sigma_t] \tag{6}$$

When the horizontal tensile stress reaches the tensile strength $[\sigma_t]$ of the damaged rock beam, cracks propagate downward and rapidly penetrate from the top to the bottom of the beam under high stress, causing the fixed-fixed beam to fracture entirely along both end sections and transform into a simply supported rock beam. Therefore, the tensile strength limit of the rock beam directly determines the critical span for

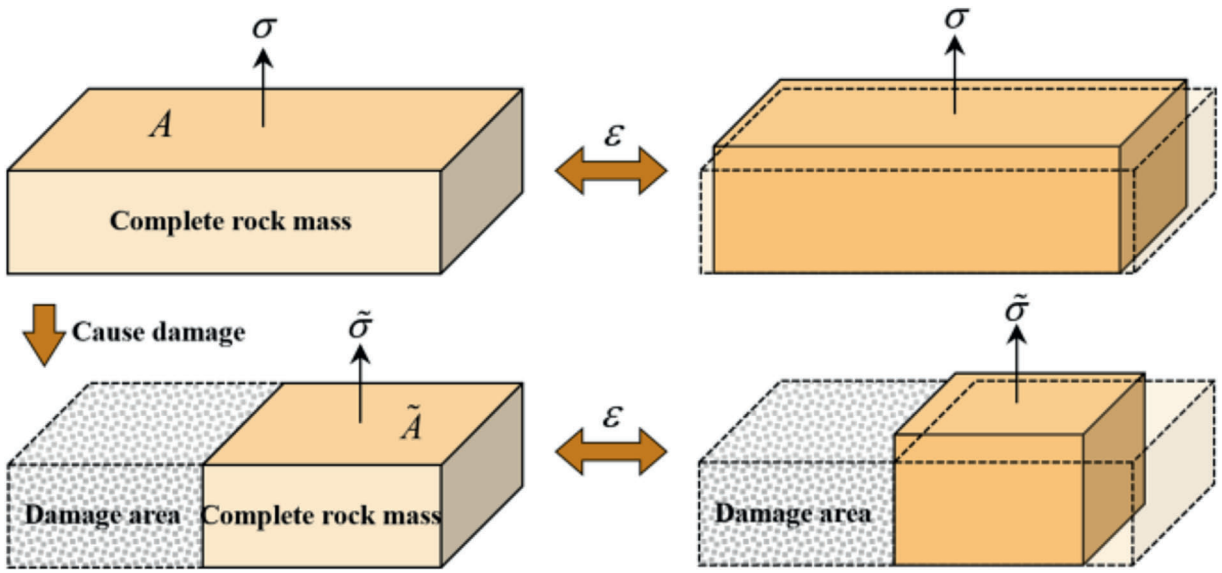

Fig. 5. Rock mass damage equivalent strain hypothesis.

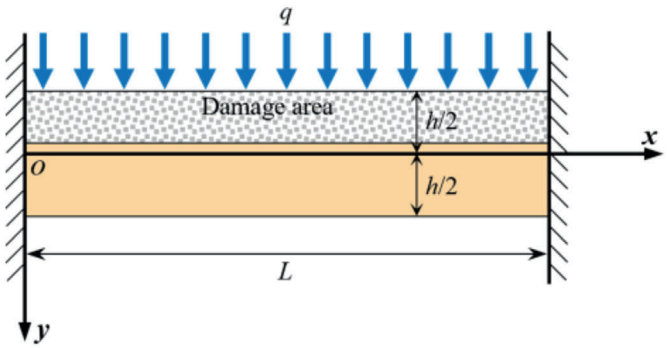

Fig. 6. Mechanics model of fixed-fixed beam for first fracture of damaged main roof.

the first roof fracture. Substituting the coordinates (0, –h/2) into Eq. (5), the critical collapse span for the first main roof fracture is obtained as,

$$L_f = h\sqrt{\frac{2[\sigma_t](1-\xi D)}{q} + \frac{2+11\nu}{5}} \tag{7}$$

Based on Eq. (7), a functional model was established with the damage variable D as the independent variable and the main roof fracture step length-to-thickness ratio (L_f/h) as the dependent variable. The variation patterns of (L_f/h) under different values of q (1 MPa, 2 MPa, 3 MPa, 4 MPa, and 5 MPa), [σ_t] (2 MPa, 3 MPa, 4 MPa, 5 MPa, and 6 MPa), and ξ (1, 0.8, 0.6, 0.4, and 0.2) were analyzed, as illustrated in Fig. 8.

Results indicate that: ① The fracture step length decreases with increasing damage variable D; ② With increasing damage correction coefficient ξ, the fracture step length becomes more sensitive and exhibits greater reduction; ③ Lower uniformly distributed load q results in a higher rate of change in fracture step length, making the beam more susceptible to damage; ④ Higher tensile strength [σ_t] leads to a larger step length for the first main roof fracture.

(2) Analysis of periodic fracture damage state of main roof

As the working face advances continuously until the main roof experiences periodic fracture, the roof is fixed at one end and free at the other. Therefore, the periodic fracture of the main roof can be simplified as a 2D cantilever beam model, as illustrated in Fig. 9.

Based on elastic mechanics theory, the horizontal stress within the cantilever beam is obtained as shown in Eq. (5) (Xie et al., 2022),

$$\sigma_x = \frac{qy}{h^3}\left(4y^2 - 6x^2 - \frac{3h^2}{5}\right) \tag{8}$$

Similar to the fixed-fixed beam, Eq. (8) indicates that the uniformly distributed load q on the cantilever beam only modifies the stress magnitude without altering its distribution pattern. Using parameters consistent with those in previous analyses, the horizontal stress distribution within the cantilever beam is derived.

As shown in Fig. 10, during bending deformation under uniform load, pronounced stress concentrations occur at the top and bottom of the fixed end of the cantilever beam. The stress gradient attenuation rate along the beam height direction is higher than that along the beam axis. With increasing span length, the peak stress within the beam increases accordingly.

Comprehensive analysis reveals that the maximum tensile stress occurs at (L, –h/2). Substituting this into Eq. (8) and combining with Eq. (6), the critical collapse span for the periodic fracture damage state of the main roof is obtained as,

$$L_p = h\sqrt{\frac{[\sigma_t](1-\xi D)}{3q} + \frac{1}{15}} \tag{9}$$

According to Eq. (9), a consistent functional model is established to analyze the variation patterns of L_p/h under different values of q, [σ_t], and ξ.

Fig. 11 demonstrates that: ① The periodic fracture step length of the damaged main roof is substantially smaller than the first fracture step length; ② Higher damage correction coefficients ξ result in greater variations in fracture step length and more severe main roof damage; ③ With increasing load q, the amplitude of fracture step length variation decreases, reducing sensitivity; ④ With increasing damage variable D, higher tensile strength [σ_t] results in a steeper reduction rate in fracture step length.

3.4. Stability analysis of equilibrium structures in damaged main roof interlayers

Key block instability is primarily manifested in two forms: sliding instability and rotational instability (Wang et al., 2019). This section investigates the critical loads for instability of the damaged main roof under these two scenarios.

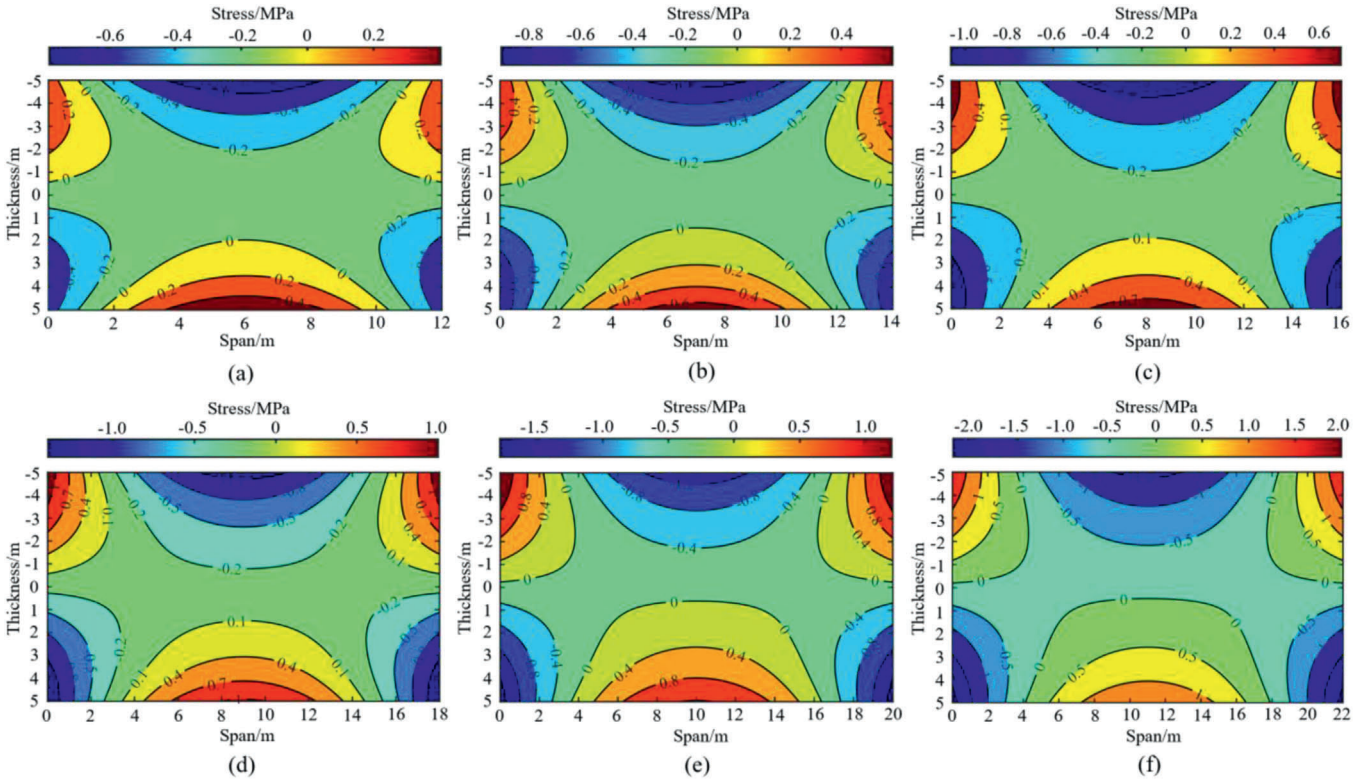

Fig. 7. Horizontal stress distribution in fixed-fixed beams with different spans. (a) $L = 12$ m, (b) $L = 14$ m, (c) $L = 16$ m, (d) $L = 18$ m, (e) $L = 20$ m, and (f) $L = 22$ m.

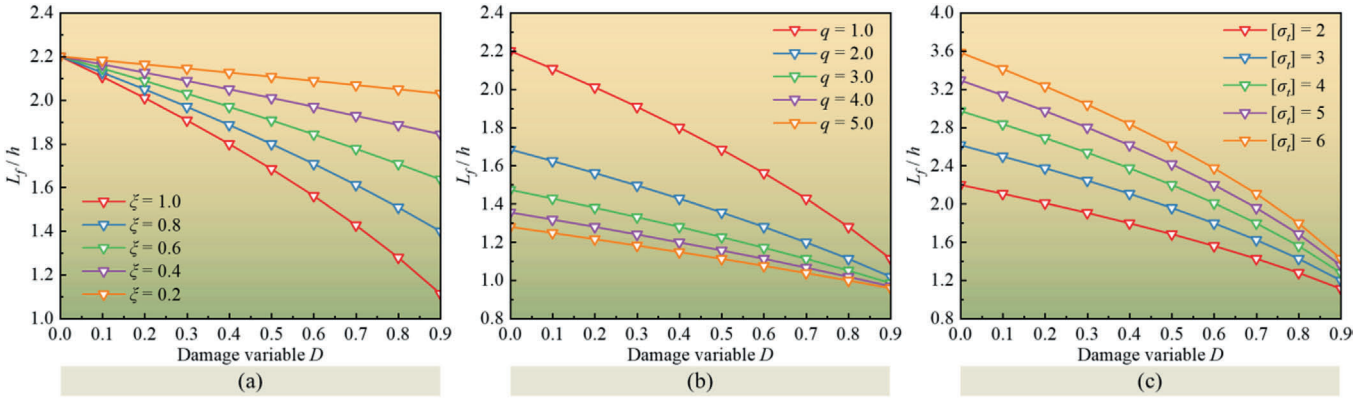

Fig. 8. First fracture step length-to-thickness ratio of interlayer damaged main roof. (a) Variation relationship between L_f/h and D under different ξ, (b) Variation relationship between L_f/h and D under different q, (c) Variation relationship between L_f/h and D under different $[\sigma_t]$.

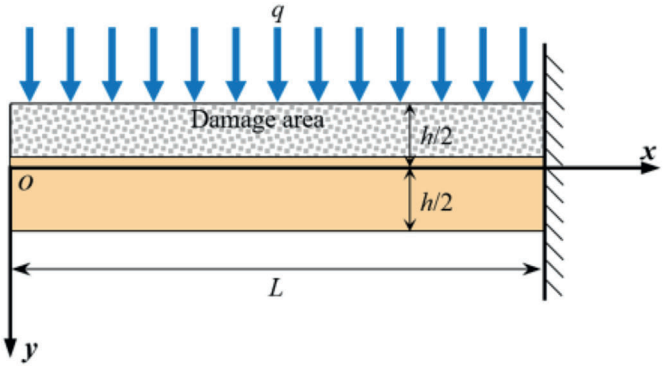

Fig. 9. Mechanics model of cantilever beam for periodic fracture of damaged main roof.

(1) Sliding instability of key block

The critical lumpiness i_s for sliding instability of the main roof is given by Eq. (10) (Xie et al., 2022), where α is the rotational angle of the rock block and $\tan\varphi$ denotes the rock block friction coefficient (typically taken as 0.3).

$$i_s = \frac{\sin\alpha + \tan\varphi(\sin\alpha \cdot \tan\alpha + \cos\alpha)}{1 - \tan\alpha \cdot \tan\varphi} \tag{10}$$

Based on the definition of lumpiness and combining Eqs. (7) and (10), the critical load expression for sliding instability during the first fracture of the interlayer damaged main roof is derived as (Xie et al., 2022),

$$q_i = \frac{10 i_s^{\,2}[\sigma_t](1 - \xi D)}{5 - i_s^{\,2}(2 + 11\nu)} \tag{11}$$

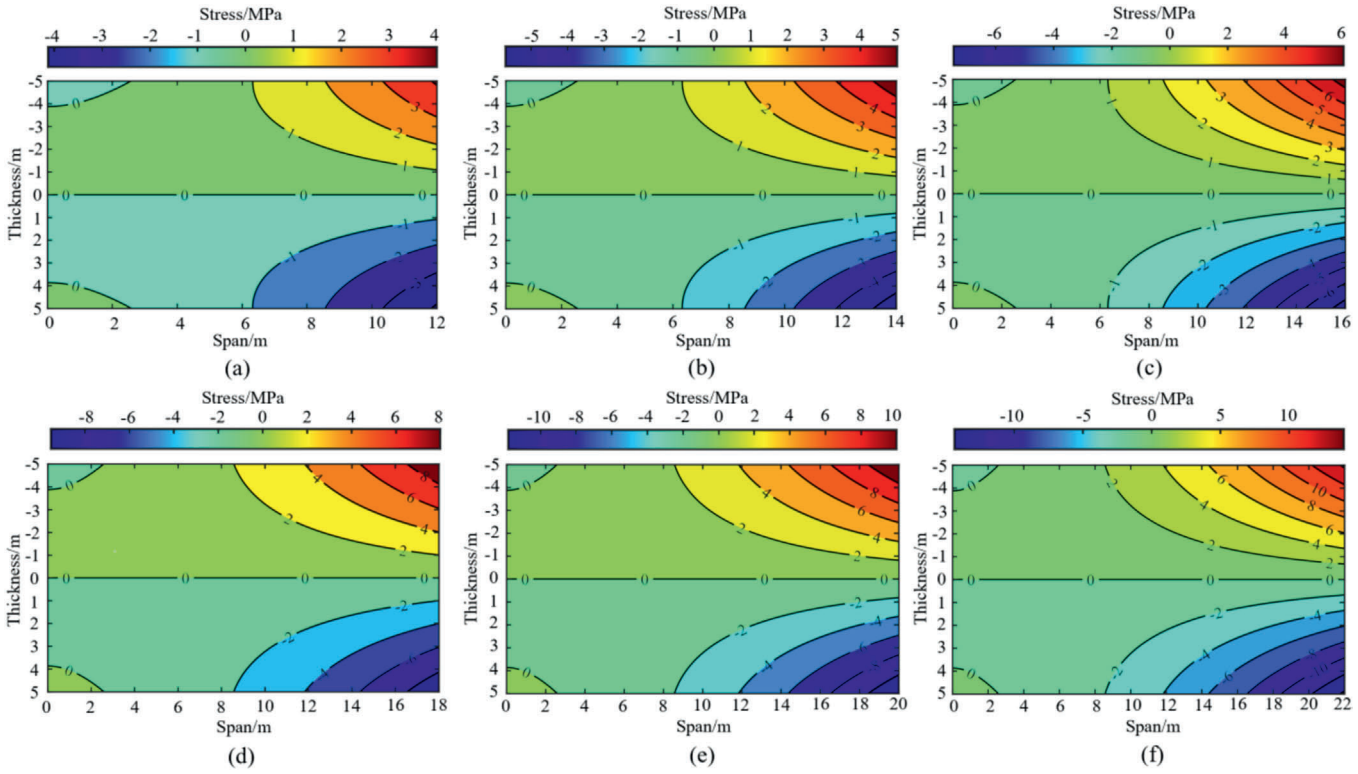

Fig. 10. Horizontal stress distribution in cantilever beams with different spans. (a) $L = 12$ m, (b) $L = 14$ m, (c) $L = 16$ m, (d) $L = 18$ m, (e) $L = 20$ m, and (f) $L = 22$ m.

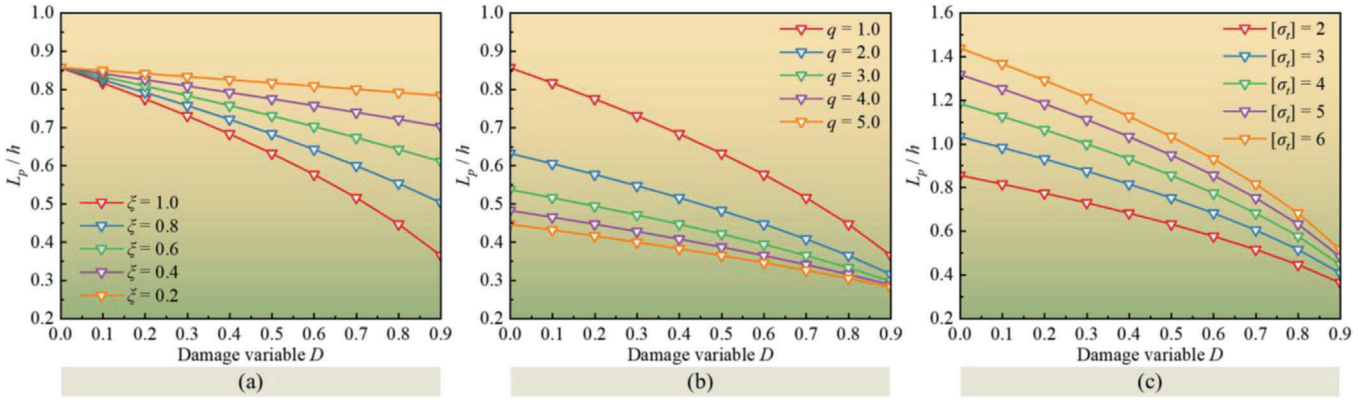

Fig. 11. Periodic fracture step length-to-thickness ratio of interlayer damaged main roof. (a) Variation relationship between L_p/h and D under different ξ, (b) Variation relationship between L_p/h and D under different q, (c) Variation relationship between L_p/h and D under different $[\sigma_t]$.

According to Eq. (11), the variation patterns of critical load q_i with damage variable D under different values of ξ, $[\sigma_t]$, and α are presented in Fig. 12.

Critical load q_i exhibits a linear decrease with increasing damage variable D, and larger damage variable coefficients accelerate the degradation of the main roof's bearing capacity. When $[\sigma_t]$ increases from 2 MPa to 6 MPa, the critical load for first fracture increases threefold. At smaller values of rotational angle α, the reduction in q_i is insignificant; however, as α increases, the sensitivity of q_i increases, leading to a steeper decline.

Similarly, the critical load expression for sliding instability during the periodic fracture of the interlayer damaged main roof is derived as,

$$q_p = \frac{5{i_s}^2[\sigma_t](1-\xi D)}{15-{i_s}^2} \tag{12}$$

The variation patterns of critical load q_p with damage variable D are illustrated in Fig. 13.

The critical load for periodic fracture sliding instability of the interlayer damaged main roof exhibits a linear distribution pattern similar to the first fracture sliding instability critical load, albeit with significantly smaller values. This indicates that under identical conditions, the instability load of the damaged main roof only exhibits numerical variations under different parameter influences while maintaining consistent variation trends.

(2) Rotational instability of key block

The critical load q_r for rotational instability of the main roof is given by Eq. (13), where η is the end angle extrusion coefficient (typically taken as 0.3) and $[\sigma_c]$ represents the compressive strength of the rock block.

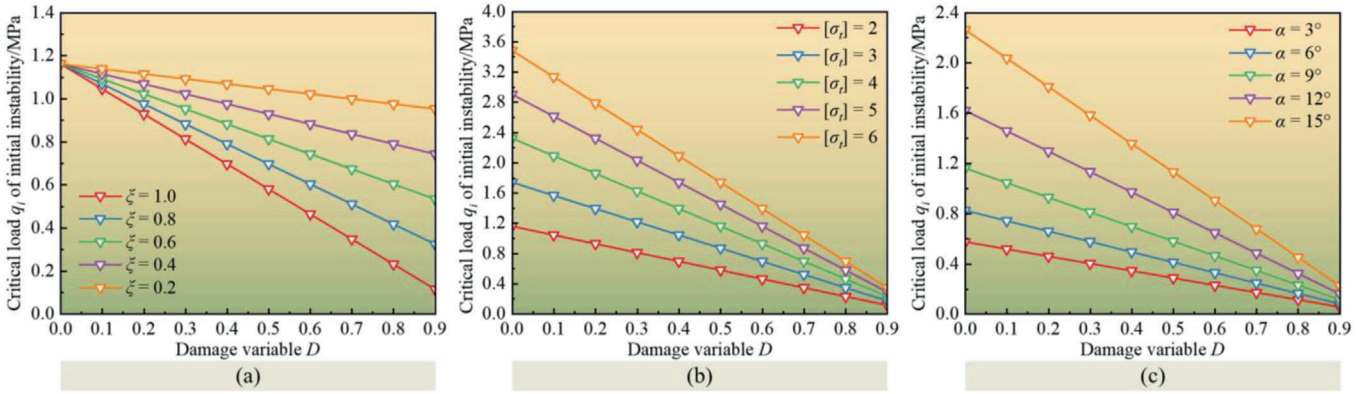

Fig. 12. First fracture sliding instability critical load of interlayer damaged main roof. (a) Variation relationship between q_i and D under different ξ, (b) Variation relationship between q_i and D under different $[\sigma_t]$, (c) Variation relationship between q_i and D under different α.

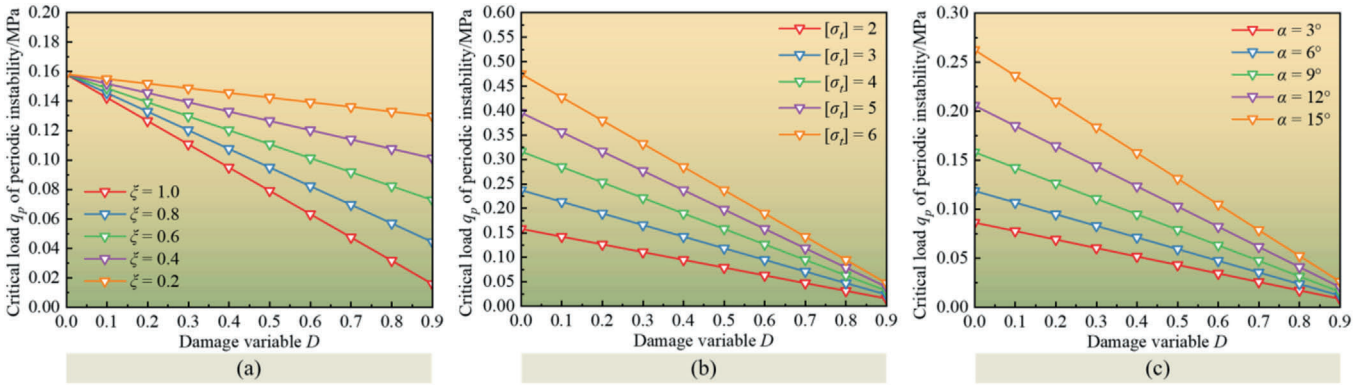

Fig. 13. Periodic fracture sliding instability critical load of interlayer damaged main roof. (a) Variation relationship between q_p and D under different ξ, (b) Variation relationship between q_p and D under different $[\sigma_t]$, (c) Variation relationship between q_p and D under different α.

$$q_r = \frac{\eta[\sigma_c](1-\xi D)(i-\sin\alpha)^2}{2[\cos\alpha + (i+\sin\alpha)\tan\alpha]} \tag{13}$$

As shown in Fig. 14, the critical load q_r for rotational instability of the damaged main roof decreases monotonically with increasing damage variable D. Smaller values of lumpiness result in smaller variation amplitudes of the instability critical load, while q_r gradually decreases as the rotational angle α increases.

In summary, the damage evolution of rock blocks significantly affects the stability of the key voussoir beam bearing structure in the main roof. Rock block damage notably increases the probability of sliding and rotational instability in the main roof's voussoir beam structure. Therefore, working faces with damaged voussoir beam structures require adequate support strength to ensure safety.

4. Stability analysis of fully mechanized top coal caving roadway based on 3DEC

4.1. Construction of 3DEC numerical model and simulation scheme

To investigate the combined effects of different main roof fracture line positions and variable section coal pillar widths on the stability of

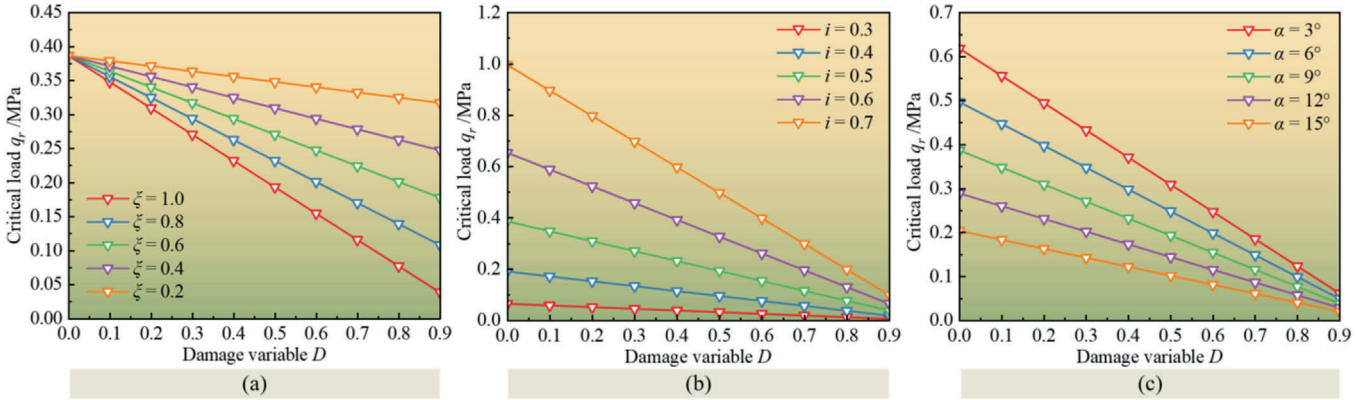

Fig. 14. Rotational instability critical load of interlayer damaged main roof. (a) Variation relationship between q_r and D under different ξ, (b) Variation relationship between q_r and D under different i, (c) Variation relationship between q_r and D under different α.

the 26110 fully mechanized caving coal roadway, a 3D computational analysis model was established using 3DEC discrete element software based on actual geological conditions, as illustrated in Fig. 15.

The model dimensions were 180 m (length) × 70 m (width) × 72.7 m (height), with fixed normal displacements applied to all boundaries and the base. A vertical load of $q = 5.05$ MPa was applied to the model top to simulate overburden weight based on the actual burial depth. Voronoi polygons were used for uniform mesh refinement near the roadway surrounding rock to effectively capture failure mechanisms influenced by roof fracture positions and coal pillar widths. The Mohr-Coulomb constitutive model was adopted for rock masses, with Coulomb slip models applied to inter-block joints.

The 26110 tailgate is affected by the overlying goaf and mining activities of the adjacent 26112 working face. The fracture morphology of the main roof exhibits significant spatial variability, and the fracture position directly determines the stress transfer path and the type of load borne by the roadway. Combined with on-site borehole peeping, characteristics of mining pressure manifestation, and theoretical analysis, the fracture positions of the main roof are mainly concentrated in four key areas: above the goaf, above the coal pillar, above the roadway, and above the solid coal. Based on orthogonal experimental design principles, numerical simulation scenarios considered two factors: fracture line positions and coal pillar widths. Five coal pillar widths (8 m, 10 m, 12 m, 14 m, 16 m) were combined with the four positions to create twenty 3D models. The controlled variable method was used to analyze how different fracture line positions affected roadway stability at each coal pillar width. The physical and mechanical parameters of each rock stratum, after being measured in laboratory tests and analyzed for strength reduction based on the damage evolution characteristic model, are detailed in Table 1.

4.2. Vertical stress evolution patterns of coal pillars under different main roof fracture configurations

Following excavation completion of each model, vertical stress distribution characteristics under different main roof fracture modes for five coal pillar widths were compiled based on 3D numerical simulation

Table 1
Mechanical parameters of coal and rock strata.

Rock stratum	K/GPa	G/GPa	φ_m/°	C_m/MPa	σ_{tm}/MPa
Medium grained sandstone	7.84	6.90	39	3.42	2.21
Carbonaceous mudstone	4.32	2.85	32	2.73	1.77
Mudstone	4.49	2.82	31	2.77	1.80
Coal seam	4.70	2.42	29	2.60	1.69
Coarse grained sandstone	6.67	5.00	36	2.95	1.91
Siltstone	6.57	5.56	37	3.28	2.12
Fine grained sandstone	5.21	4.24	34	3.11	2.01

K Bulk modulus; G Shear modulus; φ_m Friction angle; C_m Cohesion; σ_{tm} Tensile strength.

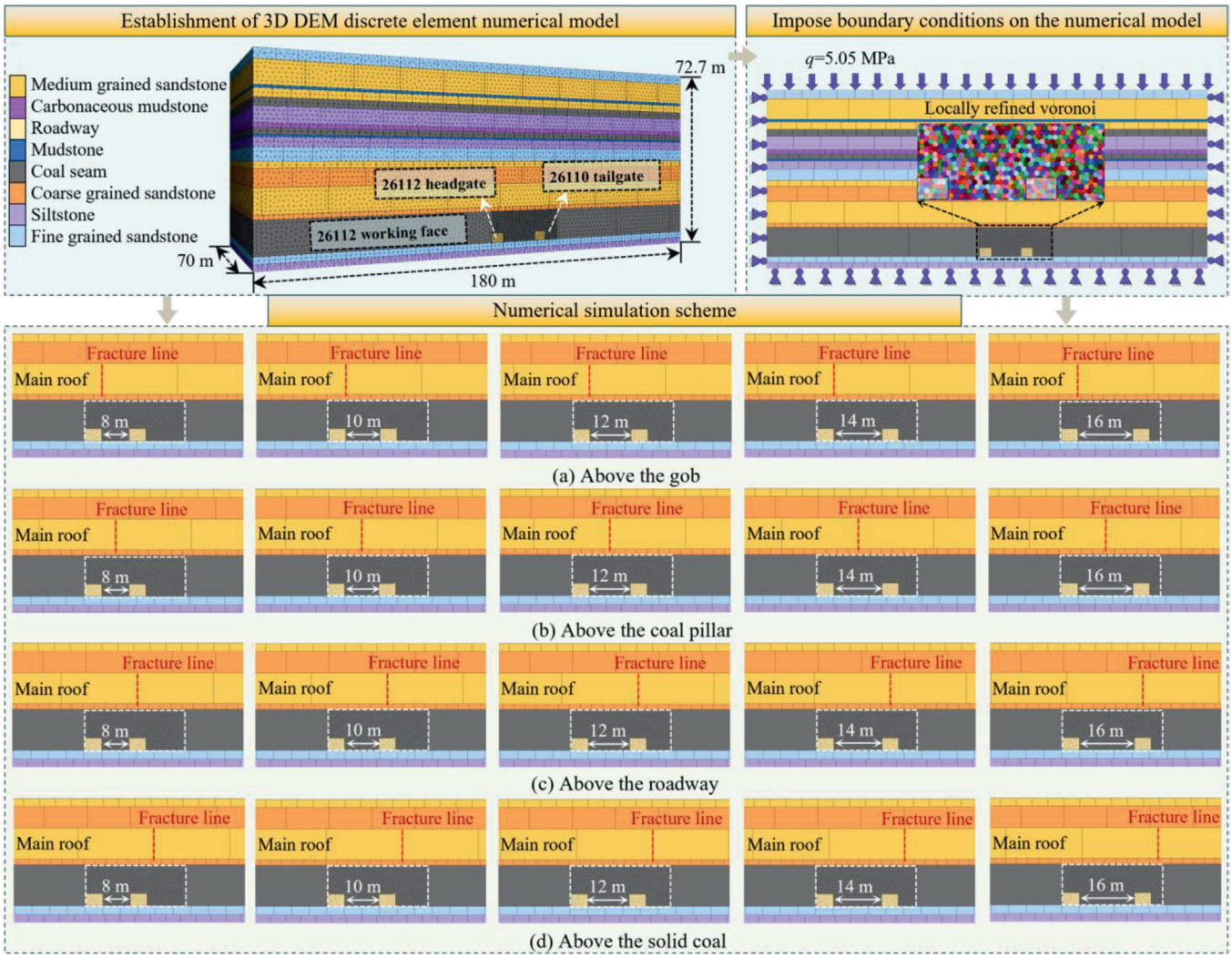

Fig. 15. Establishment of 3DEC discrete element numerical model.

results, as illustrated in Fig. 16.

At smaller coal pillar widths, vertical stress exhibited a "single-peak" pattern within the coal pillar. With increasing coal pillar width, a "double-peak" stress distribution formed, where the peak stress on the gob side of the coal pillar exceeded that on the mining side. During the transition from 8 to 16 m coal pillar widths, roadway side stresses continuously decreased when the fracture line was positioned above the gob, coal pillar, or roadway. However, when the fracture line was located above the solid coal, significant stress concentration occurred at a 10 m pillar width. To quantitatively compare stress evolution patterns under each scenario, horizontal measurement lines were established at different heights in the roadway, and relationships between peak stress, stress concentration coefficients, fracture line positions, and coal pillar widths are depicted in Fig. 17.

Based on four different fracture line scenarios, during the increase of coal pillar width from 8 m to 16 m, peak stresses in the coal pillar side of the roadway decreased by 35.5%, 37.9%, 40.0%, and 26.5% respectively, while peak stresses in the solid coal side decreased by 38.9%, 39.3%, 43.3%, and 41.1% respectively. Stress concentration coefficients followed a similar trend to peak stress variations, with higher stress concentrations observed at smaller pillar widths (8 m, 10 m). Notably, comparable stress loads were recorded for the same pillar width under different fracture line positions, indicating that the influence of fracture line location on roadway surrounding rock stress distribution was less significant compared to pillar width. The rotational collapse of the main roof at different positions did not cause substantial extrusion deformation to the coal pillars.

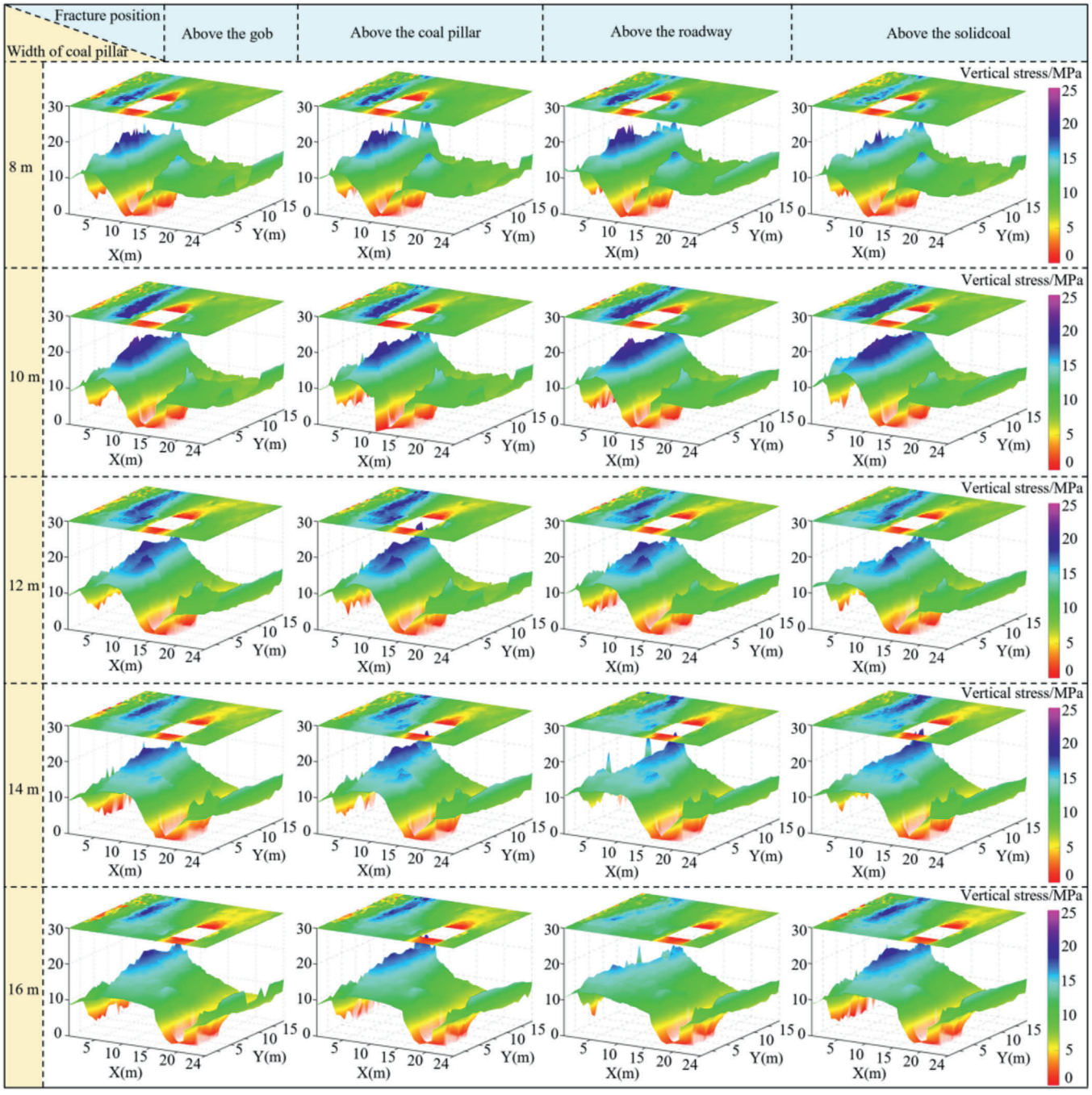

Fig. 16. Vertical stress evolution contour maps of coal pillars.

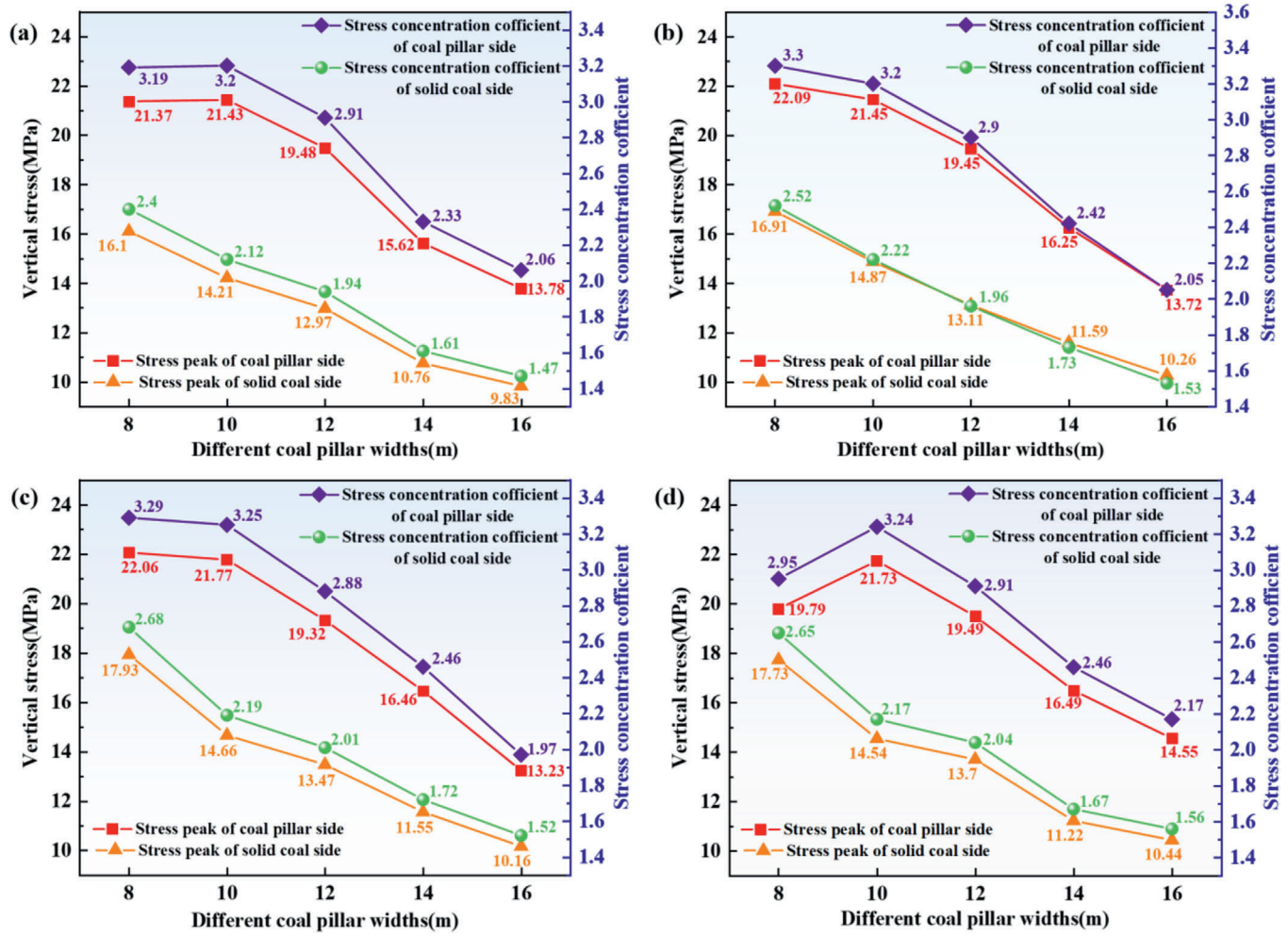

Fig. 17. Comparative analysis of vertical stress evolution patterns in coal pillars (a) The fracture line is located above the goaf, (b) The fracture line is located above the coal pillar, (c) The fracture line is located above the roadway, and (d) The fracture line is located above the solid coal.

4.3. J_2 evolution patterns of coal pillars under different main roof fracture configurations

In elastoplastic mechanics, the expression of the second invariant of the deviatoric stress tensor J_2 is:

$$J_2 = \frac{1}{6}\left[(\sigma_1-\sigma_2)^2+(\sigma_2-\sigma_3)^2+(\sigma_3-\sigma_1)^2\right] \tag{14}$$

where σ_1, σ_2, and σ_3 are the maximum, intermediate, and minimum principal stresses, respectively. Its physical meaning is to comprehensively characterize the deviatoric stress state at a point within the object. Compared with a single principal stress component, J_2 more comprehensively reflects the driving effect of the stress state on material yielding, and serves as a key indicator for determining whether a material enters the plastic state. The stress state of a rock mass can be decomposed into a spherical stress tensor and a deviatoric stress tensor, which correspond to the volume deformation and shape deformation of the rock mass, respectively. The spherical stress tensor only induces volume change, while the deviatoric stress tensor is the fundamental cause of shear deformation and plastic failure. According to the theory of plastic mechanics, when the effect of the deviatoric stress tensor exceeds the shear strength of the material, the rock mass will undergo plastic failure. The Mises yield criterion is established based on J_2, which indicates that J_2 is directly related to the yielding behavior of the material (Wu et al., 2024, 2025). J_2 distribution characteristics under different main roof fracture modes for five coal pillar widths are presented in Fig. 18.

J_2 concentration zones were formed within the coal pillar following adjacent working face mining. For narrow pillar widths (8 m–10 m), high J_2 peak zones appeared at the right rib shoulder and left rib shoulder pocket of the roadway. With increasing width (12 m–16 m), under the influence of the adjacent goaf, a narrow peak zone developed from the bottom of the goaf-side pillar to its central top. Mining-induced stress on the roadway surrounding rock gradually decreased, resulting in more uniform stress distribution with shallow annular patterns. Quantified J_2 variations along horizontal measurement lines in the roadway are shown in Fig. 19.

Stress perturbations induced by roadway excavation resulted in asymmetric J_2 distributions, with peak values on the coal pillar rib consistently exceeding those on the solid coal rib. This disparity renders the coal pillar rib more susceptible to progressive plastic zone expansion under mining influence, though the peak difference diminishes with increasing pillar width. For fracture configurations (a), (b), and (c), J_2 peaks decreased with increasing pillar width. When fractures occurred above solid coal, the 10 m pillar width exhibited the highest J_2 peak (75.19 MPa^2) at the coal pillar rib, followed by gradual reductions. Stress field evolution analysis indicated that within stress perturbation zones, J_2 peak variations displayed non-steady fluctuations, while stress reduction rates stabilized outside these zones. Overall, increasing coal pillar width reduced the J_2 stress influence domain, progressively stabilizing the roadway surrounding rock.

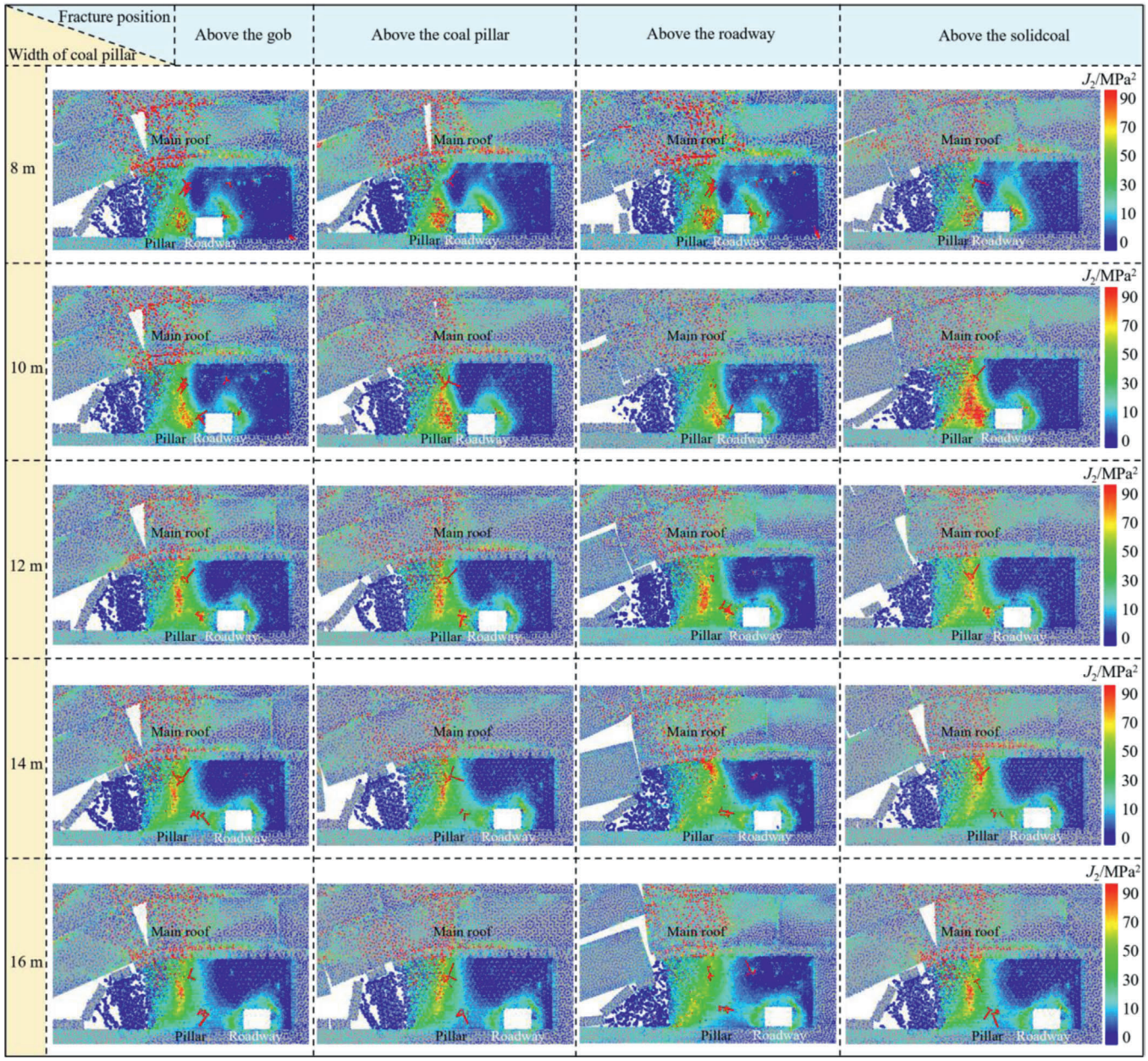

Fig. 18. J_2 evolution contour maps of coal pillars.

4.4. *Plastic zone distribution characteristics*

Plastic zones serve as a quantitative measure to compare and analyze surrounding rock failure under different fracture line positions and coal pillar widths. Plastic zone distribution characteristics for each scenario are illustrated in Fig. 20, where "None" indicates no failure occurred, "shear-p" refers to "Failure in shear in the past", "tension-p" refers to "Failure in tension in the past", and "tension-n" refers to "Failure in tension now".

The extent of plastic zones in surrounding rock decreases with increasing coal pillar width, with the most significant changes occurring on the coal pillar side. For 8 m and 10 m pillar widths, plastic zones in the roadway surrounding rock interconnected with gob-side plastic failure zones, resulting in vertical roof plastic failure zone extensions of 3.4 m–4.1 m. When pillar width increased to 12 m, plastic zone distributions began to converge, and the coal pillar developed an elastic core with enhanced load-bearing capacity and no through-going plastic zones. Visualizations in Fig. 20 clearly demonstrate the influence of pillar width on plastic zone spatial distribution, while no significant correlation were observed between main roof fracture line positions and plastic zone morphologies.

To quantitatively analyze the mechanisms of different fracture line positions, the roadway surrounding rock was divided into three characteristic regions: coal pillar zone, roof zone, and solid coal zone. Using FISH language embedded in 3DEC, plastic zone volumes in these regions were extracted and statistically analyzed. Quantitative comparison results are shown in Fig. 21.

The degree of plastic damage in the coal pillar and roof zones decreases with increasing coal pillar width. During the increase from 8 m to 16 m pillar widths under different fracture line positions, an inflection point is observed at 12 m in the solid coal zone, where plastic damage is minimized. When fractures occur above the roadway or solid coal, narrow pillars ($\leq$10 m) exhibit extensive plastic damage zones, with plastic damage percentages exceeding 80% in the coal pillar zone. Fracture line positions show weak correlation with coal pillar plastic responses as pillar width changes. With increasing distance from the

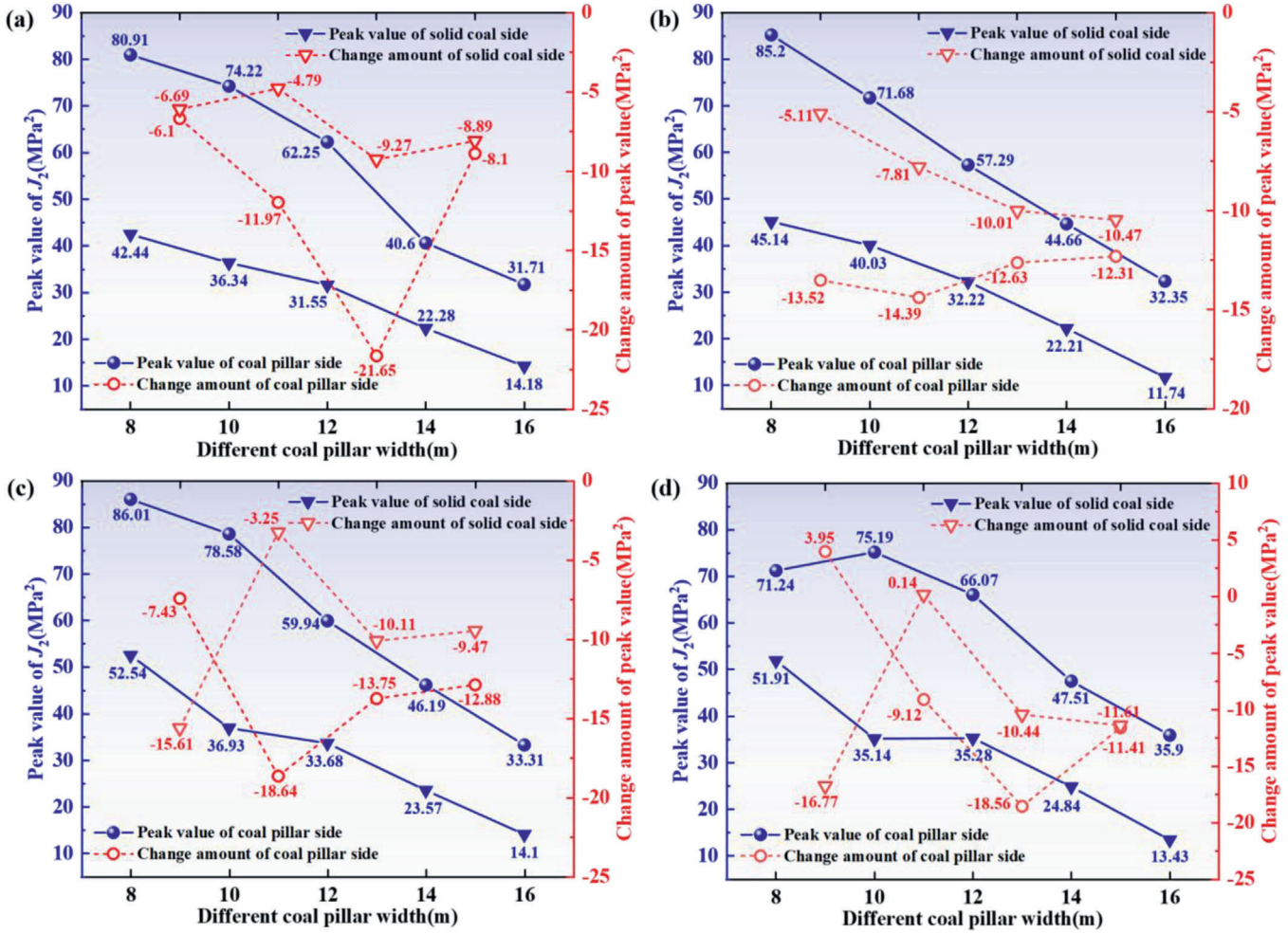

Fig. 19. Comparative analysis of J_2 evolution patterns in coal pillars, (a) The fracture line is located above the goaf, (b) The fracture line is located above the coal pillar, (c) The fracture line is located above the roadway, and (d) The fracture line is located above the solid coal.

goaf, stress gradient attenuation reduces the rate of plastic damage evolution.

Based on the above analysis, due to the roadway being affected by multiple mining disturbances, narrow coal pillar roadways exhibit significant stress concentration, and their plastic zones are prone to connect with the goaf, requiring frequent maintenance. They may even cause working face shutdown due to instability, which instead increases safety costs. In contrast, wide coal pillars will significantly reduce economic benefits. Therefore, the optimal coal pillar width is determined to be 12 m.

5. Support control of roadways with multiple-damaged surrounding rock

5.1. Support parameter design of roadway

Based on the above research, a 12 m coal pillar width was identified as the optimal design, ensuring both the full-life stability of roadways and safety production requirements. For the geological conditions of the 26,110 tailgate, the "scientific support and economic rationality" principle was adopted to optimize support parameters, with the detailed scheme shown in Fig. 22. Key technical parameters are as follows: (1) Roof support employs Φ 21.8 × 12,000 mm large-diameter high-strength prestressed steel strand cable bolts with 250 × 250 × 16 mm matching trays, spaced at 1800 × 1800 mm. Each roof bolt row consists of 6 Φ 20 mm × 2400 mm bolts spaced at 900 mm × 900 mm, with one steel ladder beam per row. (2) Rib bolts are Φ 18 mm × 2000 mm in size, arranged in 6-bolt rows (3 per side) with 1300 × 900 mm spacing. All bolts use 125 × 125 × 10 mm butterfly-shaped steel trays. Both roof and rib surfaces are reinforced with hexagonal wire mesh.

5.2. Analysis of supporting prestressed field

Fig. 23 illustrates the spatial distribution patterns of the prestressed field formed by the bolt-cable combined support system. Simulation results indicate that: Shallow surrounding rock forms a continuous three-dimensional compressive stress zone under bolt anchorage, significantly enhancing radial constraint stress on the rock surface, improving shallow rock confining pressure, and effectively controlling roof delamination. Long cables generate a compressive stress field in deep surrounding rock through stress diffusion effects, notably increasing the self-bearing capacity of deep rock. This combined long-short bolt-cable support system creates a uniform and stable load-bearing arch structure in both shallow and deep rock through stress field superposition, greatly ensuring roadway stability.

5.3. Borehole observation into cracks in surrounding rock

Borehole observation was conducted to monitor fracture development characteristics in the roadway roof rock mass during mining operations, as illustrated in Fig. 24. Results indicated that: Micro-damage existed within the shallow surrounding rock zone (0 m–0.5 m), with

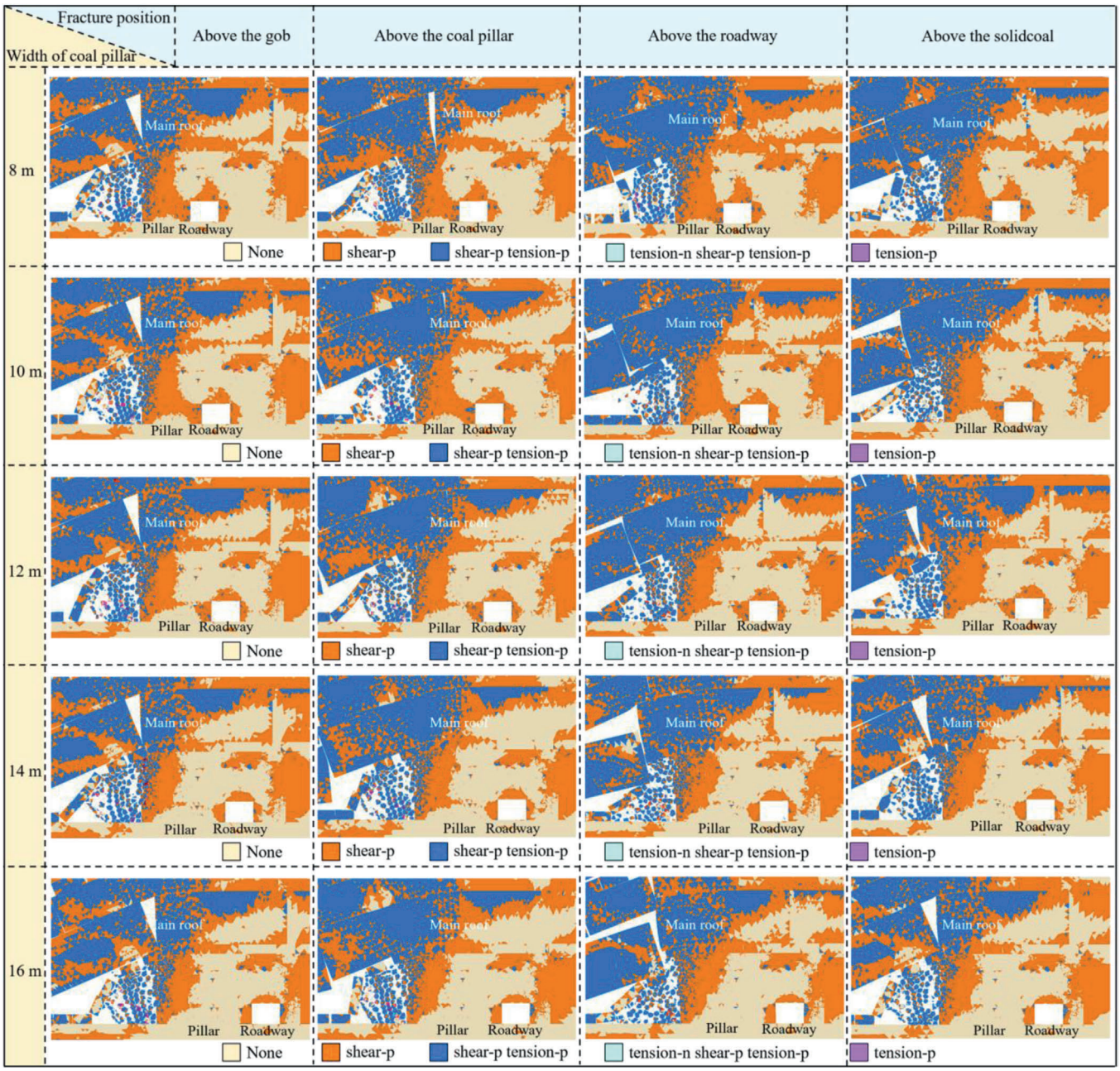

Fig. 20. Plastic zone distribution characteristics of coal pillars.

minor fractures developing up to 1.4 m depth. Isolated longitudinal fractures were observed at 3.6 m depth. From 3.6 m to 7.7 m depth, borehole walls remained smooth without fractures or weak planes, indicating high rock mass integrity. A relatively rough borehole wall was encountered at 7.7 m depth, while the coal-rock interface at 8.6 m and deeper zones exhibited intact walls with no visible fractures. Overall, rational support measures confined fractures to the shallow rock mass, preserving high integrity in deep coal-rock formations.

5.4. Field engineering practice

Monitoring stations were deployed at 100 m, 150 m, and 200 m ahead of the working face to measure roof separation, bolt-cable forces, and surrounding rock deformation, as illustrated in Fig. 25.

(1) Within the advance abutment pressure influence zone, significant displacements occurred between deep and shallow base points. Maximum displacements at deep points for the three stations were 37 mm, 49 mm, and 52 mm, with average rates of 0.55 mm/d, 0.63 mm/d, and 0.53 mm/d respectively. Shallow point maximum displacements reached 25 mm, 28 mm, and 38 mm, with average rates of 0.33 mm/d, 0.37 mm/d, and 0.39 mm/d. Maximum separation values were 12 mm, 21 mm, and 14 mm, indicating overall low roof separation levels and effective fracture suppression by the support measures.

(2) Bolt-cable forces exhibited a general increasing trend. Outside the dynamic pressure zone, forces remained stable due to greater distance from the working face. As the face advanced, forces gradually increased. Within a certain advance distance, cable

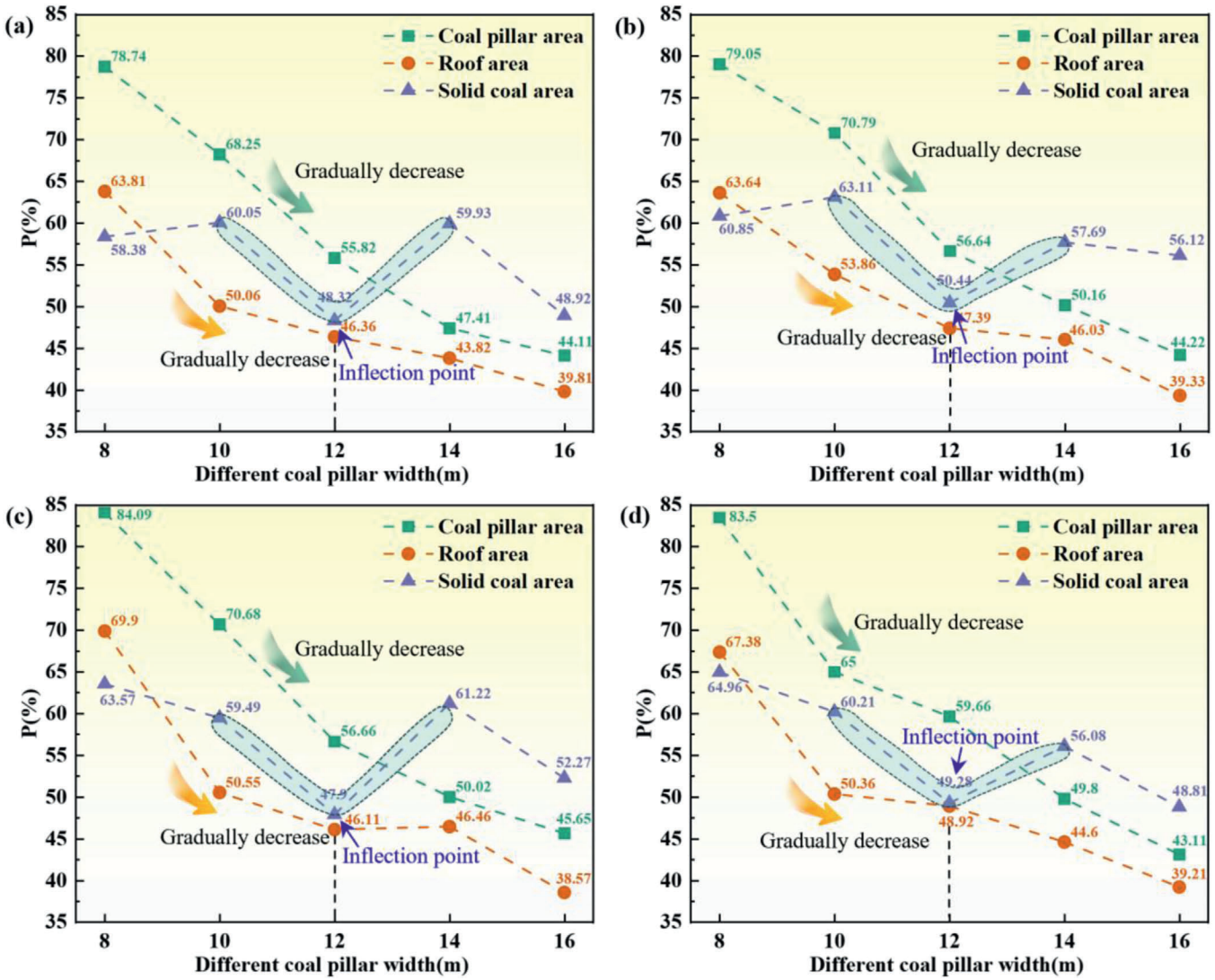

Fig. 21. Comparative analysis of plastic zone distribution characteristics in coal pillars, (a) The fracture line is located above the goaf, (b) The fracture line is located above the coal pillar, (c) The fracture line is located above the roadway, and (d) The fracture line is located above the solid coal.

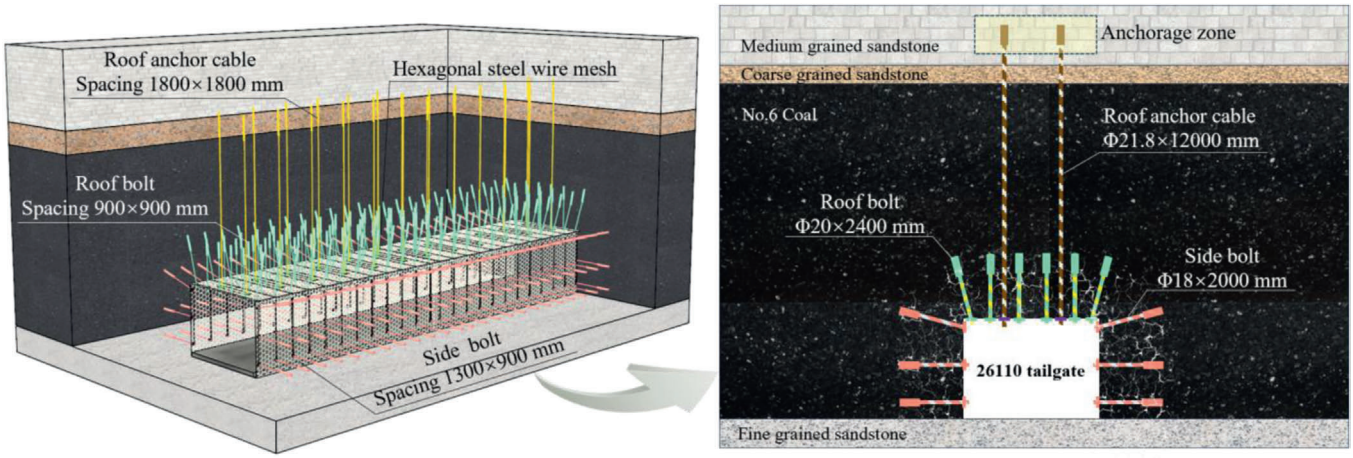

Fig. 22. Support parameters of 26110 tailgate.

forces at two stations showed abrupt increases under advance abutment pressure, with maximum values of 144.0 kN, 133.3 kN, and 148.2 kN. No abnormal conditions such as anchor withdrawal or cable rupture occurred during monitoring.

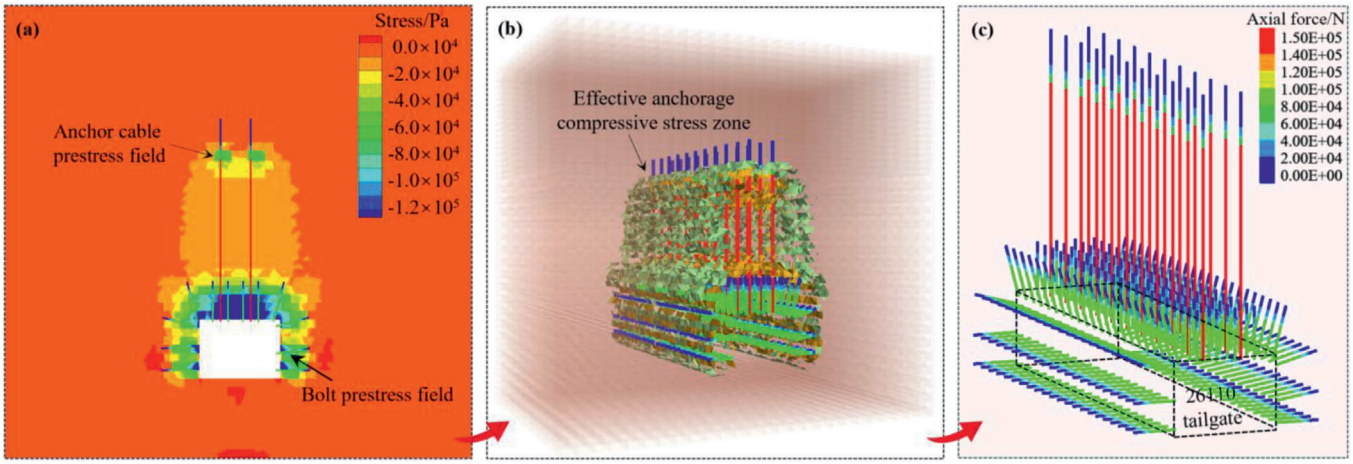

Fig. 23. Distribution of prestress field in fully mechanized top coal caving roadway, (a) Cross-section of roadway prestressed field, (b) Three-dimensional prestress field, and (c) Axial force and arrangement of anchor cables.

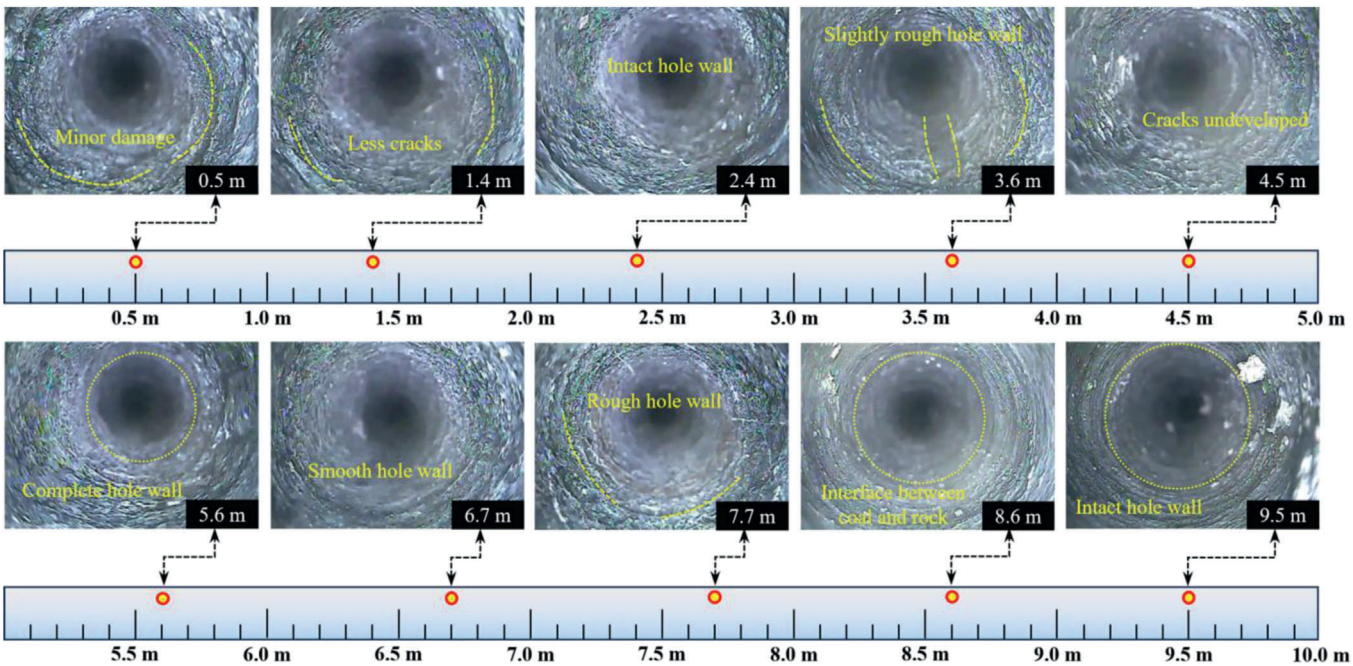

Fig. 24. Distribution characteristics of cracks in surrounding rock.

(3) High deformation rates were observed within 50 m ahead of the working face, stabilizing beyond this range. Maximum solid coal rib deformations were 318 mm, 322 mm, and 296 mm, representing increases of 58.5%, 54.8%, and 55.8% compared to static pressure sections. Roof subsidence maxima were 225 mm, 230 mm, and 200 mm, increasing by 86.0%, 87.0%, and 93.0% respectively. All convergence values remained within acceptable ranges.

Overall analysis indicates that during service, roadway ribs and roof-floor surfaces remained planar, with surrounding rock in dynamic equilibrium without instability. Field support performance is presented in Fig. 26.

6. Conclusions

(1) Based on the residual strength characteristics of rocks, a modified damage evolution characteristic model was developed to systematically reveal the mechanical correlation mechanism between damage evolution of interlayer rock mass and instability of key bearing structures under multiple coal seam repeated mining activities. The results indicate that damage to the main roof results in a reduction in both initial and periodic fracture step distances, and significantly increases the sliding and rotational instability probability of the voussoir beam structure.

(2) Through orthogonal experimental design, this study quantitatively analyzed the spatiotemporal evolution characteristics of surrounding rock stress fields and plastic zones under the coupled effects of fracture line spatial position and coal pillar width. When the coal pillar width increased from 8 m to 16 m, the peak stress on both sides of the roadway decreased by 26.5%–43.3%, the influence range of the second invariant of the deviatoric stress tensor (J_2) was reduced, and the plastic damage evolution rate decreased with increasing coal pillar width. Conversely, the fracture line position exerted a relatively weak regulatory effect on the stress-plastic response of the coal pillar.

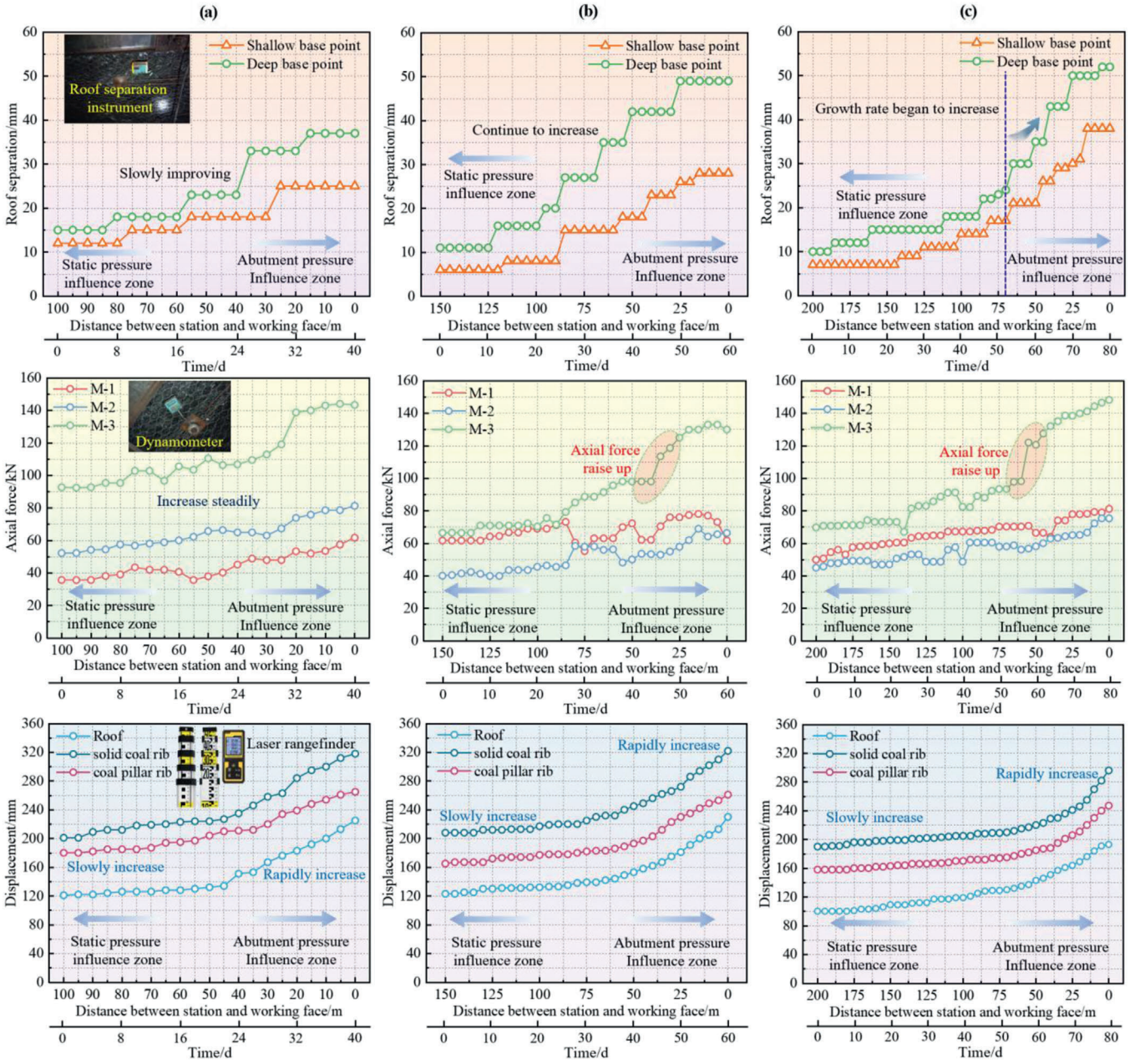

Fig. 25. Mining pressure monitoring results, (a) Station No.1 is 100 m ahead of the working face, (b) Station No.2 is 150 m ahead of the working face, and (c) Station No.3 is 200 m ahead of the working face.

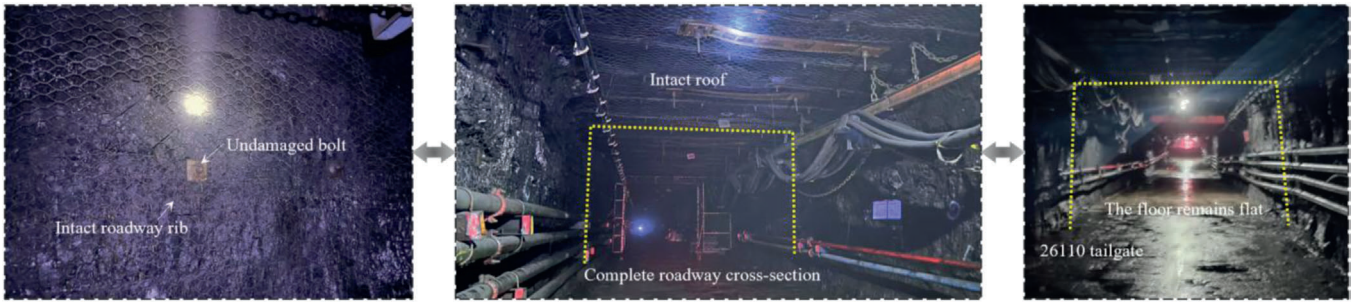

Fig. 26. Overall control performance of roadway.

(3) Based on comprehensive analysis of multiple indicators, the optimal coal pillar width was determined to be 12 m. A high-strength prestressed bolt-cable collaborative support scheme was proposed, where the radial constraint stress of shallow surrounding rock was significantly enhanced under bolt anchoring, and the bearing capacity of deep rock mass was remarkably improved under cable compressive stress. Through the superposition effect of stress fields, a homogeneous and stable load-bearing arch structure was formed in both shallow and deep surrounding rock.
(4) Field industrial tests demonstrated that the roof strata exhibited a low degree of fracture development, with deep coal-rock masses retaining high integrity. Specifically, the maximum roof separation was controlled within 21 mm, stable force distribution was maintained in the bolts and cables (maximum load 148.2 kN), and both roadway sidewall convergence and roof subsidence remained within acceptable limits. These outcomes effectively ensured safe and efficient mining operations at the working face.

CRediT authorship contribution statement

Shengrong Xie: Writing – original draft, Supervision, Funding acquisition. **Yuxuan Wang:** Writing – review & editing, Writing – original draft, Formal analysis, Data curation. **Yiyi Wu:** Methodology, Conceptualization. **Jian Yang:** Writing – review & editing, Validation. **Zhigen Wang:** Validation, Formal analysis.

Declaration of competing interest

The authors declare the following financial interests/personal relationships which may be considered as potential competing interests: Zhigen Wang is currently employed by China Coal Huayu Nanyangpo Coal Industry Co., Ltd., Shuozhou 036999, China.

Acknowledgements

This work was supported by the National Natural Science Foundation of China (No. 52074296).

Data availability

Data will be made available on request.

References

Bai, E., Guo, W., Tan, Y., 2019. Negative externalities of high-intensity mining and disaster prevention technology in China. Bull. Eng. Geol. Environ. 78 (7), 5219–5235. https://doi.org/10.1007/s10064-019-01468-4.

Chen, D., Wang, X., Wu, S., Zhang, F., Fan, Z., Wang, X., Li, M., 2023. Study on stability mechanism and control techniques of surrounding rock in gob-side entry retaining with flexible formwork concrete wall. J. Cent. South Univ. 30 (9), 2966–2982. https://doi.org/10.1007/s11771-023-5436-z.

Chen, D., Wu, Y., Xie, S., Guo, F., He, F., Liu, R., 2022. Reasonable location of stopping line in close-distance underlying coal seam and partition support of large cross-section roadway. Int. J. Coal Sci. Technol. 9 (1), 55. https://doi.org/10.1007/s40789-022-00528-7.

Cheng, G., Yang, T., Liu, H., Wei, L., Zhao, Y., Liu, Y., Qian, J., 2020. Characteristics of stratum movement induced by downward longwall mining activities in middle-distance multi-seam. Int. J. Rock Mech. Min. Sci. 136, 104517. https://doi.org/10.1016/j.ijrmms.2020.104517.

Geng, D., Fan, L., Du, Y., Zhu, Q., Li, T., Zhao, J., 2024. Research on the mechanism and control of roof deformation in gob-side entry retaining of close-distance coal seams. Eng. Fail. Anal. 164, 108682. https://doi.org/10.1016/j.engfailanal.2024.108682.

Ghabraie, B., Ren, G., Barbato, J., Smith, J.V., 2017a. A predictive methodology for multi-seam mining induced subsidence. Int. J. Rock Mech. Min. Sci. 93, 280–294. https://doi.org/10.1016/j.ijrmms.2017.02.003.

Ghabraie, B., Ren, G., Smith, J.V., 2017b. Characterising the multi-seam subsidence due to varying mining configuration, insights from physical modelling. Int. J. Rock Mech. Min. Sci. 93, 269–279. https://doi.org/10.1016/j.ijrmms.2017.02.001.

Guo, P., Yuan, Y., Ye, K., Sun, D., 2021. Fracturing mechanisms and deformation characteristics of rock surrounding the gate during gob-side entry retention through roof pre-fracturing. Int. J. Rock Mech. Min. Sci. 148, 104927. https://doi.org/10.1016/j.ijrmms.2021.104927.

Han, C., Zhang, N., Xue, J., Kan, J., Zhao, Y., 2019. Multiple and long-term disturbance of gob-side entry retaining by grouped roof collapse and an innovative adaptive technology. Rock Mech. Rock Eng. 52 (8), 2761–2773. https://doi.org/10.1007/s00603-018-1612-0.

Hu, C., Yang, X., Li, Q., Hu, B., Li, Y., Jiang, Q., Sun, F., 2024. Key parameters of gob-side entry retaining by roof cutting in close-distance seam group. Geomech. Geophys. Geo-Energy Geo-Resour. 10 (1), 55. https://doi.org/10.1007/s40948-024-00772-y.

Huang, Q., Du, J., Chen, J., He, Y., 2021. Coupling control on pillar stress concentration and surface cracks in shallow multi-seam mining. Int. J. Min. Sci. Technol. 31 (1), 95–101. https://doi.org/10.1016/j.ijmst.2020.12.019.

Lemaitre, J., Sermage, J.P., Desmorat, R., 1999. A two scale damage concept applied to fatigue. Int. J. Fract. 67–81. https://doi.org/10.1023/a:1018641414428.

Li, G., Wang, X., Bai, J., Wu, B., Wu, W., 2022a. Research on the failure mechanism and control technology of surrounding rock in gob-side entry driving under unstable overlying strata. Eng. Fail. Anal. 138, 106361. https://doi.org/10.1016/j.engfailanal.2022.106361.

Li, J., Zhang, M., Wang, C., Liao, C., Zhang, B., 2024. Failure characteristics and fracture mechanism of overburden rock induced by mining: a case study in China. Int. J. Coal Sci. Technol. 11 (1), 44. https://doi.org/10.1007/s40789-024-00693-x.

Li, Q., Wu, G., Kong, D., Han, S., Ma, Z., 2022b. Study on mechanism of end face roof leaks based on stope roof structure movement under repeated mining. Eng. Fail. Anal. 135, 106162. https://doi.org/10.1016/j.engfailanal.2022.106162.

Liu, H., Zhang, B., Li, X., Liu, C., Wang, C., Wang, F., Chen, D., 2022. Research on roof damage mechanism and control technology of gob-side entry retaining under close distance gob. Eng. Fail. Anal. 138, 106331. https://doi.org/10.1016/j.engfailanal.2022.106331.

Liu, Y., Cheng, J., Jiao, J., Gao, Z., Cheng, P., 2024a. Influences of the hard rock proportion coefficient on the evolution pattern and fractal characteristics of mining fractures in a composite roof. Int. J. GeoMech. 24 (4), 04024038. https://doi.org/10.1061/IJGNAI.GMENG-8961.

Liu, Y., Kong, D., Li, P., Wen, Z., Li, F., Zuo, Y., Wu, G., 2024b. The migration and evolution law of overlying strata and the instability and failure characteristics of end face roof under the condition of ascending mining in close distance coal seam: case study. Eng. Fail. Anal. 165, 108809. https://doi.org/10.1016/j.engfailanal.2024.108809.

Lu, C., Liu, Y., Liu, G., Zhao, T., 2019. Stress evolution caused by hard roof fracturing and associated multi-parameter precursors. Tunn. Undergr. Space Technol. 84, 295–305. https://doi.org/10.1016/j.tust.2018.11.031.

Mark, C., 2021. An updated empirical model for ground control in U.S. multiseam coal mines. Int. J. Min. Sci. Technol. 31 (2), 163–174. https://doi.org/10.1016/j.ijmst.2020.12.024.

Ning, J., Wang, J., Tan, Y., Xu, Q., 2020. Mechanical mechanism of overlying strata breaking and development of fractured zone during close-distance coal seam group mining. Int. J. Min. Sci. Technol. 30 (2), 207–215. https://doi.org/10.1016/j.ijmst.2019.03.001.

Qin, Y., Xu, N., Zhang, Z., Zhang, B., 2021. Failure process of rock strata due to multi-seam coal mining: insights from physical modelling. Rock Mech. Rock Eng. 54 (5), 2219–2232. https://doi.org/10.1007/s00603-021-02415-0.

Suchowerska Iwanec, A.M., Carter, J.P., Hambleton, J.P., 2016. Geomechanics of subsidence above single and multi-seam coal mining. J. Rock Mech. Geotech. Eng. 8 (3), 304–313. https://doi.org/10.1016/j.jrmge.2015.11.007.

Wang, F., Xu, J., Xie, J., 2019. Effects of arch structure in unconsolidated layers on fracture and failure of overlying strata. Int. J. Rock Mech. Min. Sci. 114, 141–152. https://doi.org/10.1016/j.ijrmms.2018.12.016.

Wang, F., Zhang, C., Wei, S., Zhang, X., Guo, S., 2016. Whole section anchor–grouting reinforcement technology and its application in underground roadways with loose and fractured surrounding rock. Tunn. Undergr. Space Technol. 51, 133–143. https://doi.org/10.1016/j.tust.2015.10.029.

Wang, M., Xu, Y., Xu, Q., Shan, C., Li, Z., Nan, H., Li, Y., Liu, H., Chu, T., 2023. Stability control of overburden and coal pillars in the gob-side entry under dynamic pressure. Int. J. Rock Mech. Min. Sci. 170, 105490. https://doi.org/10.1016/j.ijrmms.2023.105490.

Wang, Q., He, M., Li, S., Jiang, Z., Wang, Y., Qin, Q., Jiang, B., 2021a. Comparative study of model tests on automatically formed roadway and gob-side entry driving in deep coal mines. Int. J. Min. Sci. Technol. 31 (4), 591–601. https://doi.org/10.1016/j.ijmst.2021.04.004.

Wang, Y., Wu, G., Kong, D., Zhang, Q., 2024. Study on the destabilization and deformation breakage characteristics of the mine roof under repetitive mining of close coal seam group. Comput. Part. Mech. 11 (3), 1503–1516. https://doi.org/10.1007/s40571-023-00706-7.

Wang, Z., Li, W., Hu, Y., 2021b. Experimental study on mechanical behavior, permeability, and damage characteristics of Jurassic sandstone under varying stress paths. Bull. Eng. Geol. Environ. 80 (6), 4423–4439. https://doi.org/10.1007/s10064-021-02214-5.

Wu, X., Wang, S., Gao, E., Chang, L., Ji, C., Ma, S., Li, T., 2023. Failure mechanism and stability control of surrounding rock in mining roadway with gentle slope and close distance. Eng. Fail. Anal. 152, 107489. https://doi.org/10.1016/j.engfailanal.2023.107489.

Wu, Y., He, M., Li, H., Gao, Y., Xie, S., 2024. Instability mechanism and energy evolution of surrounding rock at intersections of deep multi-form application. J. Cent. South Univ. 31 (3), 890–911. https://doi.org/10.1007/s11771-024-5567-x.

Wu, Y., Ma, X., Chen, D., Gao, Y., Xie, S., Meng, Y., 2025. Research on the fracture mechanism and pressure relief control technology of the thick and hard roof in a coal

pillar recovery working face. Int. J. GeoMech. 25 (5), 04025063. https://doi.org/10.1061/IJGNAI.GMENG-10623.

Xie, S., Li, H., Chen, D., Feng, S., Yang, J., Ma, X., Jiang, Z., Xing, S., 2024. Research on the control technology and key parameters of external anchor-internal unloading of surrounding rock during gob-side entry driving under severe mining of 1000-m-Deep mine. Rock Mech. Rock Eng. 57 (4), 2913–2932. https://doi.org/10.1007/s00603-023-03722-4.

Xie, S., Wu, Y., Guo, F., Chen, D., Wang, E., Zhang, X., Zou, H., Liu, R., Ma, X., Li, S., 2022. Interaction mechanism of the upper and lower main roofs with different properties in close coal seams: a case study. Energies 15 (15), 5533. https://doi.org/10.3390/en15155533.

Yang, X., Wen, G., Dai, L., Sun, H., Li, X., 2019. Ground subsidence and surface cracks evolution from shallow-buried close-distance multi-seam mining: a case study in bulianta coal mine. Rock Mech. Rock Eng. 52 (8), 2835–2852. https://doi.org/10.1007/s00603-018-1726-4.

Zha, W., Shi, H., Liu, S., Kang, C., 2017. Surrounding rock control of gob-side entry driving with narrow coal pillar and roadway side sealing technology in yangliu coal mine. Int. J. Min. Sci. Technol. 27 (5), 819–823. https://doi.org/10.1016/j.ijmst.2017.07.023.

Zhang, J., Dong, X., Bai, J., Jia, L., 2024a. The mechanism and prevention of rockburst induced by the instability of the composite hard-roof coal structure and roof fractures. Eng. Fract. Mech. 310, 110512. https://doi.org/10.1016/j.engfracmech.2024.110512.

Zhang, J., Wu, J., Yang, T., Yang, S., He, Y., Gao, S., Peng, B., 2024b. Analysis of fracture evolution characteristics and formation mechanism of inter-layer rock under different mining areas. Rock Mech. Rock Eng. 57 (5), 3787–3811. https://doi.org/10.1007/s00603-023-03757-7.

Zhang, Z., Deng, M., Bai, J., Yan, S., Yu, X., 2021. Stability control of gob-side entry retained under the gob with close distance coal seams. Int. J. Min. Sci. Technol. 31 (2), 321–332. https://doi.org/10.1016/j.ijmst.2020.11.002.

Zhao, T., Gong, P., Yetilmezsoy, K., Bahramian, M., Liu, C., 2021. Dynamic failure and stability model analysis of thick and hard rock with wedge-structure immediate roof occurrence. Geomech. Geophys. Geo-Energy Geo-Resour. 7 (3), 80. https://doi.org/10.1007/s40948-021-00277-y.

Zhu, D., Tu, S., 2017. Mechanisms of support failure induced by repeated mining under gobs created by two-seam room mining and prevention measures. Eng. Fail. Anal. 82, 161–178. https://doi.org/10.1016/j.engfailanal.2017.08.029.